Modelling Simul. Mater. Sci. Eng. **21** (2013) 074007 (30pp) doi:10.1088/0965-0393/21/7/074007

A finite element simulation on transient large deformation and mass diffusion in electrodes for lithium ion batteries

Yonghao An and Hanqing Jiang

School for Engineering of Matter, Transport and Energy, Arizona State University, Tempe, AZ 85287, USA

E-mail: hanqing.jiang@asu.edu

Received 7 March 2013, in final form 18 July 2013
Published 8 October 2013
Online at stacks.iop.org/MSMSE/21/074007

Abstract

Lithium-ion batteries have attracted great deal of attention recently. Silicon is one of the most promising anode materials for high-performance lithium-ion batteries, due to its highest theoretical specific capacity. However, the short lifetime confined by mechanical failure in the silicon anode is now considered to be the biggest challenge in desired applications. High stress induced by the huge volume change due to lithium insertion/extraction is the main reason underlying this problem. Some theoretical models have been developed to address this issue. In order to properly implement these models, we develop a finite element based numerical method using a commercial software package, ABAQUS, as a platform at the continuum level to study fully coupled large deformation and mass diffusion problem. Using this method, large deformation, elasticity–plasticity of the electrodes, various spatial and temporal conditions, arbitrary geometry and dimension could be fulfilled. The interaction between anode and other components of the lithium ion batteries can also be studied as an integrated system. Several specific examples are presented to demonstrate the capability of this numerical platform.

(Some figures may appear in colour only in the online journal)

1. Introduction

Lithium-ion (Li-ion) batteries, as one type of rechargeable battery, have attracted a great deal of attention due to their high-energy density, no memory effect, reasonable life cycle and one of the best energy-to-weight ratios. They are used in applications such as portable electronic devices, satellites and potentially electric vehicles [1–3]. Among the active research occurring in electrode materials for Li-ion batteries, the development of novel electrodes that show both high-energy and high-power density is much sought after. Silicon (Si) is an attractive anode material for Li-ion batteries because it has a low discharge potential and the highest known

theoretical charge capacity of 4200 mAh g^{-1}, ten times higher than that of existing graphite anodes and other oxide and nitride materials [4]. However, the development of Si-anode Li-ion batteries has lagged behind because of the large volumetric change that occurs upon insertion and extraction of Li. During charge/discharge cycling, Li atoms diffuse in and out of the Si matrix and different Li_xSi phases are formed depending on the Li concentration. The largest volumetric change occurs for $Li_{22}Si_5$ alloy, where up to 400% volumetric change is required to accommodate 4.4 Li atoms for each Si atom, resulting in pulverization and early capacity fading of the battery cells due to the loss of electrical contact [5, 6].

The extraordinarily high-energy capacity of Si, however, has motivated researchers to explore new means that curb the limitation of Si as a practical anode material for Li-ion batteries. Exploration of Si nanostructures is one of the encouraging research directions, such as nanowires or nanotubes [4, 7–10]. High-energy capacity has been realized through these attempts, but only in the first few tens of cycles of charging and discharging and dropped quickly in the following cycles and the total cycle number is still low.

In order to improve the cyclic stability of Si anodes, the mechanism underlying the behavior of failure should be well understood in the first place. From the perspective of mechanics, the failure of lithiated Si can be attributed to the high level of lithiation induced stress [11]. It is possible that the high stress level in Si could also affect the electrochemical performance of the Si anodes [12], such as changing the working voltage of the battery and influencing the charging rate of the battery. Thus, in addition to being a key factor in understanding the failure of Si under lithiation, stress might also be an important factor that affects the performance of Li-ion batteries. Motivated by these aforementioned aspects, a large amount of work has already been conducted to examine the fundamental role of stress in Si-anode Li-ion batteries.

New novel phenomena for Si anode in Li-ion batteries have been observed in experiments. Some of them are actually beyond the traditional scope of our knowledge on the mechanical behavior of Si, such as the plasticity of lithiated Si [13]. The optical method has been used to measure the stress evolution in lithiated/delithiated Si film *in situ*. A novel feature, plasticity, has been observed in this classic material that is usually considered to be brittle [14].

From the theoretical aspect, specifically at the continuum level, various types of models have been proposed regarding the multiple mechanisms through which stress is coupled with mass diffusion. The model of diffusion induced stress can be dated back to the work by Prussin in 1960s [15], in which an analogy between diffusion induced stress and thermal stress was used. In Prussin's original work, he assumed a one-way coupling in which the diffusion of the alien particles into the matrix material produced stress in the same way as the temperature load in thermally expandable materials. This work was broadened by considering mass diffusion resulting heterogeneous materials as elastic inclusion problems, in which the inclusion energy has been incorporated into the chemical potential of migrating particles [16–18]. Thus, the coupling between mass diffusion and deformation has become two-way behavior. Explicitly, local stress level affects how fast particles could migrate into a matrix material, and in turn, the mass distribution of alien particles affects what kind of stress distribution the matrix material would take. Later, Swaminathan *et al* [19, 20] developed a strict electromechanical theory to address the diffusion induced stress problem, in which not only the elastic inclusion energy induced by the migrating defect was considered but also electrostatic energy was accounted in for charged defects. In this theory, an alien particle in a matrix material induces stress through two mechanisms, namely strain induced by the geometrical incompatibility, and Maxwell stress due to the charge carried by the particle. Recently, based on molecular dynamic simulations [21, 22], another mechanism has been proposed through which stress could affect diffusion. It is a kinetic mechanism, in which the diffusivity of an alien particle in a matrix material is exponentially dependent on the lateral

normal stress applying perpendicular to the diffusing direction. To sum up, previous studies have already shown at least four mechanisms to couple mass diffusion and deformation or stress, namely mass distribution of alien particles affecting deformation through geometric mismatch (mechanically) and carried charge (electrostatically), and stress or deformation of alien particles affecting mass diffusion through chemical potential (thermodynamically) and diffusivity (kinetically). The above mentioned studies were limited to elastic behavior of Si anode.

Motivated by recent experimental observation of plasticity of lithiated Si, there are a handful of theoretical studies incorporating Si plasticity [23, 24]. By employing nonequilibrium thermodynamics, Zhao *et al* [25] considered the coupled plastic deformation and lithiation in a spherical anode. Bower *et al* [26] developed a systematic theory to include finite deformation, diffusion, plastic flow and electrochemical reaction in the Si anode of Li-ion batteries. However, because of the complexity of these models, only simplified cases [27] were studied though the theoretical frame is somewhat complete. In order to utilize these proposed models to study more realistic situations, which include more complicated conditions, such as shapes of electrodes, mechanical and electrochemical boundary conditions with spatial and temporal complexity, as well as interaction of electrodes with different types of substrates and binders, a robust and versatile numerical platform must be developed correspondingly. To the best of our knowledge, such a numerical platform that is able to rigorously couple the important factors in electrodes, namely large deformation, mass diffusion and plasticity, is not available to the research community, though there are many related works on coupled mass diffusion and elasticity [28–31], or based on small deformation theory [32, 33]. More importantly, the numerical platform must be capable of studying the fracture and damage of electrodes, which makes this demand more challenging.

In this paper, we propose a finite element based numerical method using the commercial finite element package, ABAQUS, as a platform to study fully coupled large deformation and mass diffusion problems in electrodes. This work has two merits to differentiate it from previous studies [32]. Firstly, coupled large deformation (elasticity and plasticity) and mass diffusion is realized. The four coupling mechanisms as we previously discussed can be realized in this platform. Secondly, the implementation of this numerical method is realized via commercially available software so that the complicated mechanical and electrochemical boundary conditions can be readily imposed and electrodes with various geometries, such as three-dimensional bulk, two-dimensional thin film and one-dimensional nanowires and nanotubes can be studied. Even at the system level, the interaction between the electrode with other components in Li-ion batteries, such as current collector, substrate and binders, can be studied. Moreover, the facture and damage of electrodes can be studied through the established modules in the commercial software package, such as cohesive elements for interfacial failure. Such a numerical platform with a rigorous consideration of coupled large deformation, mass diffusion and plasticity using a commercial software package, therefore provides a robust and versatile means to study the coupled large deformation and mass diffusion in electrodes of Li-ion batteries.

This paper is organized as follows. In section 2, a general theoretical framework of coupled diffusion and large deformation is addressed. This theoretical framework will be used to develop the numerical method. Section 3 details the numerical implementation, which is based on a rigorous analogy between mass diffusion and thermal transport when large deformation presents. Section 4 presents a one-dimensional example that is studied using the present method and compared with COMSOL Multiphysics as the benchmark. Section 5 studies some practically important examples, namely Si anode bonded on current collector with and without soft binders, in which the damage and cohesive elements are involved, and the

interplay between the different failure modes in binder and anode film is investigated. Future work and application of the numerical method are discussed in section 6 as the concluding remarks.

2. Theoretical model

In this section, the theoretical model for coupled large deformation and mass diffusion in electrodes for Li-ion batteries is generalized and integrated by following the previously developed models [25, 26, 34]. The Lagrangian description is used in depicting the model. Here the physical explanations are the focus while the rigorous derivation and proof are left for the previously developed models.

2.1. Kinematics of deformation

The process of charging and discharging in Li-ion battery is the process of Li migrating in and out of electrodes, such as the Si electrode. Thus, the object of interest consists of Li and electrode and it is referred as the system. Following standard continuum mechanics, deformation gradient $\boldsymbol{F}(\boldsymbol{X}, t)$ is used to describe the deformation of the system. $\boldsymbol{X}$ is the coordinates of a material point at the reference state, which is chosen to be the state for pure electrode or completely discharged electrode. t is the time. To characterize the distribution of Li in the electrode matrix, the nominal concentration of Li $C(\boldsymbol{X}, t)$ is defined as the mole of Li per unit volume of electrode at the reference state.

It is assumed that the deformation gradient $\boldsymbol{F}$ could be polar decomposed into three parts, namely, deformations due to material's elasticity, plasticity and concentration change, respectively [25, 26]. Furthermore, these three parts could be diagonalized concurrently. Thus, the principal stretches could be decomposed into three parts, i.e. elastic, plastic and concentration parts,

$$\lambda_i = \lambda_i^{\mathrm{e}} \lambda_i^{\mathrm{p}} \lambda_i^{\mathrm{c}} \qquad (i = 1, 2, 3. \text{ No summation convention}). \tag{1}$$

Here the superscripts 'e', 'p' and 'c' denote elastic, plastic and concentration parts, respectively. The principal stretch due to concentration change is assumed to be isotropic,

$$\lambda_1^{\mathrm{c}} = \lambda_2^{\mathrm{c}} = \lambda_3^{\mathrm{c}} = \lambda^{\mathrm{c}}(C), \tag{2}$$

though it may not be valid for crystal materials, such as Si, in which the stretch due to concentration change depends on the crystal orientation [35].

2.2. Constitutive relations

Assume that the nominal free energy density of the system W can be defined as the function of the seven basic variables, λ_1^{e}, λ_2^{e}, λ_3^{e}, λ_1^{p}, λ_2^{p}, λ_3^{p} and C. Utilizing the thermodynamics inequality and incompressibility of plasticity, the chemical potential μ of Li in an electrode, and true stress σ in the Li/electrode compound could be determined by

$$\sigma_i = \frac{1}{\lambda_1 \lambda_2 \lambda_3} \frac{\partial W}{\partial \ln \lambda_i^{\mathrm{e}}}, \tag{3}$$

$$\mu = \frac{\partial W}{\partial C} - \lambda_1 \lambda_2 \lambda_3 \sigma_{\mathrm{h}} \frac{3}{\lambda^c} \frac{\mathrm{d}\lambda^{\mathrm{c}}}{\mathrm{d}C}. \tag{4}$$

Here σ_i $(i = 1, 2, 3)$ is the principal true stress and $\sigma_{\mathrm{h}} = \frac{1}{3}(\sigma_1 + \sigma_2 + \sigma_3)$ is the hydrostatic stress. The detailed derivation can be found in [25]. Equations (3) and (4) provide constitutive relations of the Li/electrode system.

In a recent work by Cui *et al* [36], in addition to the hydrostatic stress, the deviatoric stress also enters the chemical potential in the form of the Eshelby stress tensor. Moreover, the dependence of a material's mechanical property on the compositional strain makes another stress related contribution to the chemical potential. We adopt the hydrostatic stress-dependent chemical potential in the following analysis, though the general stress-dependent chemical potential could be easily implemented using a similar approach.

2.3. Material models

The nominal free energy density of the system W consists of strain energy density and chemical energy density,

$$W(\lambda_i^{\mathrm{e}}, \lambda_i^{\mathrm{p}}, C) = W_{\mathrm{s}}(\lambda_i^{\mathrm{e}}, \lambda_i^{\mathrm{p}}) + W_{\mathrm{c}}(C). \tag{5}$$

$W_{\mathrm{s}}(\lambda_i^{\mathrm{e}}, \lambda_i^{\mathrm{p}})$ is the strain energy density exclusively depending on elastic–plastic deformation. In other words, $W_{\mathrm{s}}(\lambda_i^{\mathrm{e}}, \lambda_i^{\mathrm{p}})$ is caused by the change of atomic potential of electrode atoms due to the change in their distance induced by mechanical deformation elastically or plastically. $W_{\mathrm{s}}(\lambda_i^{\mathrm{e}}, \lambda_i^{\mathrm{p}})$ vanishes when $\lambda_i^{\mathrm{e}} = \lambda_i^{\mathrm{p}} = 1$ $(i = 1, 2, 3)$. Different forms of strain energy density will give different mechanical constitutive relations. Here we decide not to specify and leave it in a general form, while the specific mechanical constitution we used in our simulation is described in the following section. $W_{\mathrm{c}}(C)$ is the chemical energy density introduced in the system due to the new chemical bonding formed between Li and electrode atoms, which depends on the electrochemical reactions, as well as the entropy increase because of mixing these heterogeneous species, which is similar to that in the solution theory. As an example, a specific form of the chemical energy density is given by the following [34],

$$W_{\mathrm{c}} = RTC_{\max}(\bar{C}\ln\bar{C} + (1-\bar{C})\ln(1-\bar{C})) + C_{\max}\bar{C}(1-\bar{C})(A_0\bar{C} + B_0(1-\bar{C})). \tag{6}$$

Here RT is the product of gas constant R and absolute temperature T (i.e. energy per mole), $C_{\max}$ is the maximum concentration that could ever be reached in the Li/electrode system, $\bar{C} = C/C_{\max}$ is the normalized concentration that is used to characterize the relative saturation level of Li in an electrode and A_0 and B_0 are two empirical parameters. The first term in equation (6) describes the mixing entropy based on ideal mixing from the solution theory, and the second term in equation (6) represents the energy of forming new chemical bonding, which is also called excess energy, accounting for deviation from ideal behavior of mixing. The excess energy reflects the existence of different Li/electrode phases at different Li concentrations, which depends on the process of electrochemical reactions. It should be noted that it is not necessary to take the form suggested by equation (6), which is specifically called the three-suffix Margules model [37]. In fact, different forms, such as the Van Laar model and Wilson model, have been developed and other empirical parameters (similar to A_0 and B_0) have been employed. One must realize that accurate modeling needs to use more realistic excess energy for the Li/electrode system and thus detailed information on the phase transition of the Li/electrode system is important.

Recent experiments have revealed that the lithiation process always involves a sharp phase boundary between Li rich and Li poor phases [38–40]. The motion of the phase boundary is isotropic in amorphous Si while anisotropic in crystal Si [41]. The current numerical approach can be extended for the diffusion controlled phase boundary problem, though the numerical simulation of these phenomena is not within the scope of this work. The basic idea is to follow the phase-field method to model the coexistence of two phases. A free energy with double well has to be constructed by choosing the proper parameters A_0 and B_0 in the excess energy (equation (6)). In order to suppress the instability at the interface, the interface energy between two phases will be introduced. To consider the anisotropic motion of the phase boundary, the

orientation dependence of surface energy can be introduced. A similar idea has been used by Hong and Wang [42]. Different from the diffusion controlled interface motion as discussed above that can be easily realized through a slight modification of our numerical platform, the reaction controlled phase boundary motion cannot be implemented by a simple modification of the present platform. A separate paper on the reaction controlled phase boundary motion is in preparation by the same authors.

Substituting equation (6) into equation (4), the chemical potential per mole is given as

$$\mu = RT \ln \frac{\bar{C}}{1-\bar{C}} - [2(A_0 - 2B_0)\bar{C} - 3(A_0 - B_0)\bar{C}^2] - \lambda_1\lambda_2\lambda_3\sigma_h \frac{3}{\lambda^c}\frac{\mathrm{d}\lambda^c}{\mathrm{d}C}. \tag{7}$$

The first term is the driving force for Li diffusion, which urges Li to diffuse from places with high concentration to places with low concentration; the second term depends on the quadratic term of Li concentration and thus prefers to keep Li in a pre-determined state depending on the two empirical parameters A_0 and B_0, which leads to phase separation; and the third term reflects the influence of stress on the chemical potential, which can be understood by the analogy of a pipette, i.e. a negative pressure 'pumping in' and a positive pressure 'squeezing out'.

The $\mathrm{d}\lambda^{\mathrm{c}}/\mathrm{d}C$ term actually defines a coefficient of compositional expansion, similar to the coefficient of thermal expansion. As a simple model, the stretch due to the change in Li concentration is assumed to be linearly dependent on Li concentration,

$$\lambda^{\mathrm{c}}(C) = 1 + \beta\bar{C}. \tag{8}$$

Here β is the non-dimensional coefficient of compositional expansion, which can be determined by the maximum volumetric change of the electrode during charge and discharge.

It is noticed that different volume expansion has been suggested, such as linear dependence of volume change on concentration [43–45]. Before more accurate experimental measurement, these two forms of compositional expansion are both reasonable. We adopt equation (8) in the following analysis, though other expressions of compositional expansion can be similarly implemented.

2.4. Mechanical constitution

The model/numerical approach is neither limited to any particular mechanical constitution, nor is this paper focused on the topic of a realistic mechanical constitution. In fact, one would find the present numerical platform in this paper is compatible with most of the standard or user-defined mechanical models. In order to provide a completed model description, a simple elastic–plastic mechanical constitution is given here and used throughout our simulation. The logarithm strain is adopted as the strain measurement here, which is commonly used as the strain measurement in the updated Lagrangian description for nonlinear finite element analysis.

The elastic property of the material is assumed isotropic, with the constitutive relation in the principal directions as

$$\sigma_i = \frac{E}{1+\nu}\left(\ln\lambda_i^{\mathrm{e}} + \frac{\nu}{1-2\nu}(\ln\lambda_1^{\mathrm{e}} + \ln\lambda_2^{\mathrm{e}} + \ln\lambda_3^{\mathrm{e}})\right), \tag{9}$$

where E, ν are Young's modulus and Poisson's ratio of the Si anode. For a small time increment in an updated Lagrangian description, this elastic constitutive relation recovers the linear Hook's law.

The von Mises yielding criterion is adopted for the plastic deformation as

$$\sigma_{\mathrm{v}} = \sigma_{\mathrm{Y}}(\ln\lambda_{\mathrm{eq}}^{\mathrm{p}}), \tag{10}$$

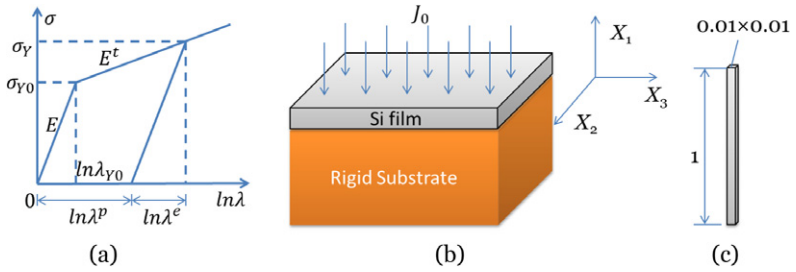

Figure 1. (*a*) A bilinear elastic–plastic strain–stress curve for uniaxial tensile testing. (*b*) Illustration of a silicon thin film on a rigid substrate lithiated by constant flux. (*c*) Geometry used to model the system in ABAQUS and COMSOL.

where σ_{v} is the von Mises stress and defined by

$$\sigma_{\mathrm{v}} = \sqrt{\tfrac{1}{2}[(\sigma_1 - \sigma_2)^2 + (\sigma_2 - \sigma_3)^2 + (\sigma_3 - \sigma_1)^2]} \tag{11}$$

and σ_{Y} is the material's yielding stress, which could be described as follows when a linear stress hardening law is assumed

$$\sigma_{\mathrm{Y}}(\ln \lambda^{\mathrm{p}}_{\mathrm{eq}}) = \sigma_{\mathrm{Y0}} + E^{\mathrm{p}} \ln \lambda^{\mathrm{p}}_{\mathrm{eq}}. \tag{12}$$

Here σ_{Y0}, E^{p} are the initial yielding stress and the 'plastic' modulus, respectively, and $\ln \lambda^{\mathrm{p}}_{\mathrm{eq}}$ is the equivalent plastic strain that characterizes the accumulated plastic deformation during the deformation history, defined by

$$\ln \lambda^{\mathrm{p}}_{\mathrm{eq}} = \ln \lambda^{\mathrm{p}}_{\mathrm{eq}}\Big|_{t=0} + \int_0^t \sqrt{\frac{2}{3}\frac{\mathrm{d}(\ln \lambda^{\mathrm{p}}_i)}{\mathrm{d}t}\frac{\mathrm{d}(\ln \lambda^{\mathrm{p}}_i)}{\mathrm{d}t}}\,\mathrm{d}t. \tag{13}$$

The incremental plastic strain is determined by the flow rule,

$$\Delta \ln \lambda^{\mathrm{p}}_i = \Delta\alpha(t)(\sigma_i - \sigma_{\mathrm{h}}) \tag{14}$$

and

$$\Delta\alpha(t) = \begin{cases} \Delta\alpha > 0, & \text{for } \dfrac{\mathrm{d}\sigma_{\mathrm{v}}}{\mathrm{d}t} > \dfrac{\mathrm{d}\sigma_{\mathrm{Y}}}{\mathrm{d}t},\ \sigma_{\mathrm{V}} = \sigma_{\mathrm{Y}}, \\ 0, & \text{otherwise} \end{cases} \tag{15}$$

is a time-dependent scalar which could be determined by the boundary value problem.

Figure 1(*a*) illustrates a bilinear strain–stress curve under uniaxial tension as an example of the aforementioned constitutive relations. In uniaxial tension, $\sigma_{\mathrm{v}} = \sigma$, $\ln \lambda^{\mathrm{p}}_{\mathrm{eq}} = \ln \lambda^{\mathrm{p}}$ and the tangential modulus is given by

$$E^{\mathrm{t}} = \frac{1}{(1/E^{\mathrm{p}}) + (1/E)}. \tag{16}$$

2.5. Governing equations and boundary conditions

The governing equations for the coupled large deformation and mass diffusion include mechanical equilibrium and mass conservation law as follows:

$$\frac{\partial \sigma_{ij}}{\partial x_i} = 0, \tag{17}$$

$$\frac{\partial C}{\partial t} + \frac{\partial J_K}{\partial X_K} = 0. \tag{18}$$

The mechanical equilibrium is written in terms of true stress σ_{ij} and current coordinates x_i, at the current time t. The mass conservation law is expressed in terms of the nominal concentration C, nominal mass flux J_K and the reference coordinates X_K, at the current time t. The detailed derivations can be found elsewhere [26]. It should be noted that the usually used conservation law in small deformation,

$$\frac{\partial c}{\partial t} + \frac{\partial j_k}{\partial x_k} = 0 \tag{19}$$

written using true quantities (true concentration c and true flux j_k) and current coordinates x_k, does not hold for large deformations.

Various boundary conditions for the coupled deformation and mass diffusion could be imposed, including stress or displacement boundaries for mechanical deformation and flux or concentration boundaries for mass diffusion. Specifically for Li-ion battery problems, a meaningful boundary condition is the prescribed flux condition in reference coordinates,

$$J_K N_K = \bar{J} \quad \text{on } S_f, \tag{20}$$

where $\bar{J}$ is the prescribed flux over a surface S_f with the outward normal direction N_k in the reference state. Equation (20) stands for the constant electrical current condition under which the battery is charging or discharging, or galvanostatic charging or discharging.

2.6. Kinetics

Similarly, the kinetic law describing the mass flux of Li into the electrode is given in terms of nominal quantities [26] other than true ones, as

$$J_I = -C M_{IJ} \frac{\partial \mu}{\partial X_J}, \tag{21}$$

where M_{IJ} is the mobility tensor, as a measurement of how fast Li diffuses in the electrode matrix. Here one should note that since the nominal flux $\boldsymbol{J}$ is used, the coordinates (I and J) in equation (21) refer to the initial coordinates.

An alternative way to define flux in finite deformation theory is to assume that the true flux is proportional to the true gradient of chemical potential at the current state. These two definitions coexist in the literature [26, 45] and both have their own merits. In terms of implementation, one can easily switch from one to the other using the numerical platform in this paper. In addition, the mobility tensor M_{IJ} can be connected through the deformation gradient with the diffusivity tensor in the current state, which can be measured experimentally or determined from *ab initio* calculation.

Suggested by Haftbaradaran *et al* [22, 34], the lateral pressure perpendicular to the direction of diffusion could affect the diffusivity, working in a way similar to frictional force. Therefore, a stress-dependent mobility tensor is adopted and its nonzero components are

$$\begin{aligned} M_{11} &= M_0 \exp\left(\kappa \frac{S_{22} + S_{33}}{2}\right), \\ M_{22} &= M_0 \exp\left(\kappa \frac{S_{11} + S_{33}}{2}\right), \\ M_{33} &= M_0 \exp\left(\kappa \frac{S_{11} + S_{22}}{2}\right). \end{aligned} \tag{22}$$

Here M_0 is the mobility at a stress-free state, κ is an empirical parameter describing the coupling between stress and diffusivity and S_{IJ} is the second Piolar–Kirchhoff stress. The second Piolar–Kirchhoff stress is used since the mobility tensor is defined in the reference state.

The two-way coupling of deformation and mass diffusion is thus realized in this section, specifically the hydrostatic stress term in chemical potential (equation (7)), and the stress-dependent mobility (equation (22)). No Maxwell stress is involved since the electrostatic interaction between Li and electrode matrix is not considered in this paper.

3. Numerical method

In order to utilize the theoretical model as presented in section 2, a robust and versatile numerical method must be developed correspondingly. In addition to the development of an in-house code [46], a numerical method that is based on commercial software may be more powerful and easier to disseminate in the community. In this section, we will present a rigorous numerical method to implement the theoretical model in section 2 in a commercial finite element package, ABAQUS. Here ABAQUS is chosen because of its wide use in the mechanics community.

The mechanical deformation, both elasticity and plasticity under large deformation, can be modeled in ABAQUS via its well-developed modules. Therefore, this section does not discuss the implementation of the mechanical deformation in ABAQUS but focuses on the coupled mechanical deformation and mass diffusion under large deformation in ABAQUS, since this coupling is not yet readily available in ABAQUS.

3.1. Dimensionless description of mass diffusion

A dimensionless formulation is used. The energy per mole is normalized by RT (unit: J mole^{-1}); mole density is normalized by $C_{\max}$ (unit: mole m^{-3}); length is normalized by a characteristic length L in the problem considered; and time is normalized by L^2/D_0, where $D_0 = M_0 RT$ (unit: m^2 s^{-1}) is diffusivity of Li in the electrode matrix in a stress-free state. Thus, the following dimensionless quantities are defined: Li concentration $\bar{C} = C/C_{\max}$, time $\tau = D_0 t/L^2$, coordinates $\bar{X}_K = X_K/L$, $\bar{x}_i = x_i/L$, stress $\bar{\sigma}_{ij} = \sigma_{ij}/C_{\max}RT$, chemical potential $\bar{\mu} = \mu/RT$, flux $\bar{J} = (L/C_{\max}D_0)J$, mobility tensor $\bar{\boldsymbol{M}} = (RT/D_0)\boldsymbol{M}$ and other parameters $\bar{A}_0 = A/RT$, $\bar{B}_0 = B/RT$, $\bar{\kappa} = \kappa C_{\max}RT$.

Based on equation (18), the dimensionless mass conservation law becomes

$$\frac{\partial \bar{C}}{\partial \tau} + \frac{\partial \bar{J}_K}{\partial \bar{X}_K} = 0, \tag{23}$$

and dimensionless nominal flux is obtained from equation (21),

$$\bar{J}_K = -\bar{M}_{KL}\left\{\left[\frac{1}{1-\bar{C}} - 2(\bar{A}_0 - 2\bar{B}_0)\bar{C} + 6(\bar{A}_0 - \bar{B}_0)\bar{C}^2 + \frac{3\beta^2\bar{C}\det \boldsymbol{F}\bar{\sigma}_{\mathrm{h}}}{(1+\beta\bar{C})^2}\right]\frac{\partial \bar{C}}{\partial \bar{X}_L} - \frac{3\beta\bar{C}}{1+\beta\bar{C}}\frac{\partial}{\partial \bar{X}_L}(\det \boldsymbol{F}\bar{\sigma}_{\mathrm{h}})\right\}. \tag{24}$$

3.2. An analogy between mass diffusion and heat transfer

The analogy between these two transport phenomena, namely mass diffusion and heat transfer, has been realized and utilized dating back to Prussin in 1960s [15] when coupled deformation and mass diffusion was studied, though it was for small deformations. This analogy must be carefully examined for large deformation, specifically for the implementation in ABAQUS.

The governing equation for heat transfer in ABAQUS is

$$\rho\frac{\mathrm{d}U}{\mathrm{d}T}\frac{\partial T}{\partial t} + \frac{\partial f_i}{\partial x_i} = r, \tag{25}$$

where ρ is the density, U is the heat energy, T is the temperature, t is the time, f_i is the true heat flux and r is the production of heat source. It should be noted that this equation is written at current coordinates $\boldsymbol{x}$. However, it is by no means an Eulerian description but an updated Lagrangian description that is used when a large deformation is considered in ABAQUS.

To compare with equation (25), the mass conservation law (equation (23)) using the total Lagrangian description is expressed in the current configuration as

$$\frac{1}{\det \boldsymbol{F}}\frac{\partial \bar{C}}{\partial \tau} + \frac{\partial}{\partial \bar{x}_i}\left(\frac{F_{iK}\bar{J}_K}{\det \boldsymbol{F}}\right) = 0. \tag{26}$$

By comparing equation (25) for heat transfer and equation (26) for mass diffusion, an analogy can be made for large deformation: mass diffusion is analogous to heat transfer by the following equivalence,

$$\begin{aligned} &\bar{C} = T,\\ &\tau = t,\\ &\frac{F_{iK}\bar{J}_K}{\det \boldsymbol{F}} = f_i,\\ &\frac{1}{\det \boldsymbol{F}} = \rho\frac{\mathrm{d}U}{\mathrm{d}T},\\ &r = 0. \end{aligned} \tag{27}$$

The mass diffusion problems then can be modeled as heat transfer problems in ABAQUS by defining temperature T as dimensionless concentration $\bar{C}$, time t as τ, true heat flux f_i as $F_{iK}\bar{J}_K/\det \boldsymbol{F}$, density of heat capacity $\rho(\mathrm{d}U/\mathrm{d}T)$ as $1/\det \boldsymbol{F}$ and vanishing heat source r. This specifically defined heat transfer behavior is implemented in ABAQUS via its user-defined heat transfer subroutine UMATHT.

UMATHT subroutine receives temperature T (or equivalently $\bar{C}$ in this analogy) and its spatial gradient $\partial T/\partial x_i$ (i.e. $\partial \bar{C}/\partial \bar{x}_i$) from ABAQUS and defines heat capacity per volume $\rho(\mathrm{d}U/\mathrm{d}T)$ (i.e. $1/\det \boldsymbol{F}$), heat flux f_i (i.e. $F_{iK}\bar{J}_K/\det \boldsymbol{F}$) and its derivatives respective to temperature $\partial f_i/\partial T$ and temperature gradient $\partial f_i/\partial(\partial T/\partial x_i)$. Thus in addition to the equivalence given by equation (27), the equivalence

$$\begin{aligned} &\frac{\partial f_i}{\partial T} = \frac{\partial}{\partial \bar{C}}\left(\frac{F_{iK}\bar{J}_K}{\det \boldsymbol{F}}\right),\\ &\frac{\partial f_i}{\partial(\partial T/\partial x_i)} = \frac{\partial(F_{iK}\bar{J}_K/\det \boldsymbol{F})}{\partial(\partial \bar{C}/\partial \bar{x}_i)} \end{aligned} \tag{28}$$

also needs to be included.

This user-defined heat transfer behavior depends on deformation and stress since the deformation gradient $\boldsymbol{F}$ and stresses (true stress σ and second Piolar–Kirchhoff stress $\boldsymbol{S}$) appear in the equivalence (equations (27) and (28)), which can also be realized in UMATHT through some practical techniques. It should be noted that even the deformation gradient $\boldsymbol{F}$ and stresses can be passed into UMATHT, the appearance of the gradient of stress and deformation (i.e. $\partial(\det \boldsymbol{F}\bar{\sigma}_{\mathrm{h}})/\partial \bar{X}_L$ in equation (24)) makes the implementation challenging since they are defined at the integration points not nodal variables as displacement that its derivatives can be calculated via interpolation using shape functions or the pointwise least squares (PLS) method. Appendix A details these practical techniques to implement UMATHT.

Using this user-defined heat transfer subroutine UMATHT and existing coupled deformation and heat transfer module in ABAQUS, the coupled deformation and mass diffusion can be realized in ABAQUS. To correctly implement this numerical method, the thermal expansion in heat transfer that is analogous to the compositional expansion in mass diffusion must be reconsidered in ABAQUS as we will discuss in the next subsection.

3.3. An analogy between compositional expansion and thermal expansion

The compositional expansion and thermal expansion are both eigen deformations, in which they are analogous. In Li-ion batteries, particularly for electrodes such as Si that experience large volumetric change, the compositional expansion is extremely large, up to 400% volumetric expansion for the Si electrode, which is far beyond the small deformation range for thermal expansion. Therefore, the analogy between composition expansion and thermal expansion must be carefully reexamined regarding the numerical aspect for large deformation.

Equation (8) assumes a linear compositional expansion. Using the undeformed electrode as the reference (i.e. vanishing Li concentration), at a given Li concentration $\bar{C}$ (or equivalently, temperature T using the analogy as discussed), the compositional strain is

$$\varepsilon_{\text{compositional}} = \lambda^{\text{c}} - 1 = \beta\bar{C}. \tag{29}$$

For thermal expansion, a linear relation between temperature change and thermal strain is also commonly used. For a nonlinear problem, it is solved by dividing into many incremental steps and at each increment step, e.g. at the increment step N, the thermal strain is given by

$$\varepsilon^{(N)}_{\text{thermal}} = \alpha\Delta T^{(N)}, \tag{30}$$

where α is the coefficient of thermal expansion and $\Delta T^{(N)} = T^{(N)} - T^{(N-1)}$ is the temperature increment at the current increment step N with the superscript as the number of the increment. Despite equations (29) and (30) being similar in formality, a simple equivalence cannot be established in the numerical method since different strain measurements are used.

The compositional strain equation (29) is based on a total Lagrangian description, i.e. the strain measurement is regarding the undeformed state. However, an updated Lagrangian algorithm is used in many commercial finite element packages (e.g. ABAQUS), in which the reference state is not the undeformed state and every time step is treated as a problem with an infinitesimal increment in displacement. When doing that, converged coordinates from the last time step are used as the reference state and a small Green strain at time step N is defined in the principal coordinates as

$$\varepsilon^{(N)} = \frac{\partial x^{(N)}}{\partial x^{(N-1)}} - 1. \tag{31}$$

In order to correctly express the compositional strain equation (29) as a thermal strain in ABAQUS, thermal strain must be redefined. It could be derived from equation (31) that

$$1 + \varepsilon^{(N)} = \frac{\partial x^{(N)}}{\partial x^{(0)}} \Big/ \frac{\partial x^{(N-1)}}{\partial x^{(0)}} = \lambda^{(N)}/\lambda^{(N-1)}. \tag{32}$$

Based on this equation, the thermal strain should be defined as follows:

$$\varepsilon^{(N)}_{\text{thermal}} \approx \ln\left(1 + \varepsilon^{(N)}_{\text{thermal}}\right) = \ln(1 + \beta T^{(N)}) - \ln(1 + \beta T^{(N-1)}). \tag{33}$$

This redefined thermal strain is able to correctly represent the compositional strain equation (29) and can be embedded in ABAQUS via its user-defined thermal expansion subroutine UEXPAN.

3.4. Prescribed flux boundary condition

Prescribed flux boundary condition represents an important experiment process, namely, constant current during charge and discharge, or galvanostatic charge and discharge. Depending on the mass and theoretical capacity (e.g. 4200 mAh g^{-1} for Si) of the active electrode materials, a current is pre-determined to conduct the galvanostatic charge and discharge. In the modeling, the current is actually the applied flux of Li on the surface

Table 1. Parameters used in section 4.

Parameters	Values
E, Young's modulus of Si	130 GPa
E_p, plastic modulus of Si	1.83 GPa
ν, Poisson's ratio of Si	0.3
ε_Y, yielding strain of Si	0.2%
v, molar volume of Si	$12 \times 10^{-6}\ \mathrm{m^3\ mole^{-1}}$
C_{max}, maximum nominal Li concentration	$0.3667 \times 10^{6}\ \mathrm{mole\ m^{-3}}$
R, gas constant	$8.314\ \mathrm{J\ K^{-1}\ mole^{-1}}$
T, room temperature	300 K
β, compositional expansion coefficient	0.5874
D_0, diffusivity of Li	$10^{-12}\ \mathrm{cm^2\ s^{-1}}$

of electrodes. In other words, the flux is pre-determined before the deformation and thus the prescribed flux is calculated in the undeformed state. However, the updated Lagrangian algorithm in ABAQUS uses an updating state as the reference. Thus, the prescribed flux boundary condition for the undeformed state has to be re-calculated for the current state.

Starting from the conservation of total flux

$$\bar{j}\,\mathrm{d}a = \bar{J}\,\mathrm{d}A. \tag{34}$$

Here $\mathrm{d}a$ and $\mathrm{d}A$ are the areas of an element of surface after and prior to deformation, $\bar{j}$ is the flux for the current configuration to be determined, and $\bar{J}$ is the prescribed flux calculated for the undeformed reference state. Using Nanson's formula, the deformation dependent flux for the current state is given by

$$\bar{j} = \frac{\bar{J}}{\det \boldsymbol{F}\sqrt{(N_K F_{Ki}^{-1})(N_L F_{Li}^{-1})}}. \tag{35}$$

Quantities involved in this expression are either accessible in ABAQUS or provided by users. A user subroutine UFLUX is utilized to implement this formula. Appendix A further discusses this implementation with more details.

By the implementation of the above discussed aspects, the coupled large deformation and mass diffusion in electrodes for Li-ion batteries can be rigorously realized in ABAQUS. It should be noted that a static problem with a pre-determined state of charge (SOC) only needs to redefine the thermal expansion to correctly represent the compositional expansion as discussed in section 3.3, while the transient problems have to include all the aspects discussed in this section. Appendix B gives a few examples to benchmark the numerical methods and the user subroutines involved are available upon request to the authors.

Through these examples in appendix B, it is verified that each of the three user subroutines UMAT, UEXPAN and UFLUX is properly programmed. Furthermore, in order to verify that all these subroutines work properly in a coordinated way, we set up a simple example as a benchmark by comparing results using the present approach and using COMSOL Multiphysics 4.2a.

4. Benchmark of the numerical implementation

4.1. Material parameters and element

In our simulation, we focus on the Si electrode. All the parameters used in examples in this section are listed in table 1.

It is assumed that the Si anode is amorphous, as it becomes amorphous after the first cycle of charge in experiments. The phase transformation of Si anode from crystal to amorphous during the first cycle is not considered in this paper. We assume a bilinear plastic–elastic constitutive relation for Si, as described in section 2.3. For material properties in the elastic range, we refer to the literature for amorphous Si [47] with elastic modulus $E = 130\,\text{GPa}$ and Poisson's ratio $\nu = 0.3$. However, the material properties in the plastic range are not fully available yet so that we adopt some typical values: the yielding strain $\varepsilon_\text{Y} = 0.2\%$ as a typical one for metal plasticity, and a 'plastic' modulus $E_\text{p} = 1.83\,\text{GPa}$ as a reasonable value to fit some experiments [14, 48].

In all user subroutines, both moduli and stresses are normalized by $C_\text{max}RT$ and it is estimated as follows. The volume of one mole Si atoms in solid is given by $v = M_\text{Si}/\rho_\text{Si} \approx 12 \times 10^{-6}\,\text{m}^3\,\text{mole}^{-1}$, where M_Si and ρ_Si are molar mass and density of Si, respectively. It is known that the compound with maximum Li concentration among all the possible Li/Si compounds during the electrochemical reactions is $\text{Li}_{22}\text{Si}_5$. Thus, the maximum nominal Li concentration C_max is determined by $C_\text{max} = 4.4/v = 0.3667 \times 10^6\,\text{mole}\,\text{m}^{-3}$ and $C_\text{max}RT = 0.915\,\text{GPa}$. Therefore, normalized elastic and plastic moduli are $\bar{E} = 142.15$ and $\bar{E}_\text{p} = 14.215$, which are the material parameters used in the examples presented in this paper.

It is also known that the maximum volumetric expansion for lithiated Si is as high as 400% associated with compound $\text{Li}_{22}\text{Si}_5$ [4], which determines the coefficient of compositional expansion $\beta = 0.5874$ via $(\lambda^\text{c}_\text{max})^3 = (1+\beta)^3 = 400\%$. Since this model does not consider the electrical process, the maximum capacity $4200\,\text{mAh}\,\text{g}^{-1}$ of Si does not explicitly enter the picture. The parameters A_0 and B_0 are taken to be zero as there are no meaningful reference values available.

To normalize time, the factor $t_\text{d} = L^2/D_0$ is estimated in the following. As listed in [49, 50], the diffusivity of Li in Si is $1.7 \times 10^{-11}\,\text{cm}^2\,\text{s}^{-1}$ and $6.4 \times 10^{-11}\,\text{cm}^2\,\text{s}^{-1}$ at discharge capacity of $800\,\text{mAh}\,\text{g}^{-1}$ and $1200\,\text{mAh}\,\text{g}^{-1}$, respectively (in bulk material), and $2 \times 10^{-10}\,\text{cm}^2\,\text{s}^{-1}$ at average discharge capacity of $1882\,\text{mAh}\,\text{g}^{-1}$ (in nano material). By extrapolating these data, it is estimated that the stress-free diffusivity or the diffusivity at vanishing Li concentration is $D_0 \approx 10^{-12}\,\text{cm}^2\,\text{s}^{-1}$. Therefore, for the range of characteristic length scale $L = 10\,\text{nm}$–$10\,\mu\text{m}$, the diffusion time range $t_\text{d} = 1$–$10^6\,\text{s}$.

The physical meanings for normalized time τ and flux $\bar{J}$ are the following. In normalized time $\tau = D_0 t/L^2$, the real time t has a physical meaning, such as total charge time T, e.g. 3600 s for 1 C charge rate and 360 s for 10 C charge rate, respectively; L has a physical meaning as a characteristic length scale, such as the thickness of a Si anode. Thus, for total charge time T, the corresponding normalized total charge time τ_total becomes $\tau_\text{total} = D_0 T/L^2$. For a Si anode 100 nm in thickness (i.e. $L = 100\,\text{nm}$), unit normalized total charge time (i.e. $\tau_\text{total} = 1$) actually means that it takes 100 s to fully charge this Si anode, which provides a charge rate 36 C. For the same unit normalized total charge time, it takes 10 000 s to fully charge a Si anode with 1 μm in height, which corresponds to 0.36 C. The nominal flux J, total charge time T and maximum nominal Li concentration C_max are related via

$$JAT = C_\text{max}AL, \tag{36}$$

where A is the cross-sectional area in the reference state. Considering the normalized flux $\bar{J} = (L/C_\text{max}D_0)J$ (discussed in section 3.1), one obtains that

$$\bar{J}\tau_\text{total} = 1. \tag{37}$$

Thus, a unit normalized total charge time is accompanied by a unit normalized flux on the Si anode. In the following simulations, without specific statement, all variables are normalized.

A quadratic brick element with temperature as an additional degree of freedom is used. Specifically, element C3D20T in ABAQUS is used throughout the simulations in this paper. This element has 20 nodes and 27 integration points. However, any element with coupled displacement and temperature as active degree of freedom can be utilized.

4.2. Benchmark using a simple example

For an essentially coupled multi-field problem with large deformation, elasticity and plasticity, as described in section 2, to the best of our knowledge, there is no verified numerical tool available to solve it. In order to benchmark the present numerical approach, we formulate a simple coupled problem, in which the deformation field can be explicitly determined from the concentration field. In other words, this problem is analytically decoupled and reformulated into a nonlinear diffusion problem. Therefore, this problem could be readily solved by commercial software, such as COMSOL Multiphysics through its PDE module. Meanwhile, this problem can still be treated as a coupled multi-field problem and solved by the present numerical approach. Thus, the present numerical approach is benchmarked by comparing with COMSOL Multiphysics.

The example we consider here is illustrated in figure 1(*b*), where an infinitely large thin Si film is firmly bonded on a rigid thick substrate. A uniform lithium flux J_0 is applied from the top surface of the Si thin film. The interface between the Si thin film and the rigid substrate is assumed to be impermeable to lithium. A computational model shown in figure 1(*c*) is meshed into 100 ($100 \times 1 \times 1$) quadratic elements, and used for both ABAQUS and COMSOL simulation.

Appendix C provides details of this problem with some core equations in the following. The governing equations are given by

$$\frac{\partial \bar{C}}{\partial \tau} + \frac{\partial \bar{J}_1}{\partial \bar{X}_1} = 0, \tag{38}$$

$$\bar{J}_1 = -\left[\frac{1}{1-\bar{C}} + \frac{3\beta^2 \bar{C}\lambda_1 \bar{\sigma}_{\mathrm{h}}}{(1+\beta\bar{C})^2}\right]\frac{\partial \bar{C}}{\partial \bar{X}_1} + \frac{3\beta\bar{C}}{1+\beta\bar{C}}\frac{\partial}{\partial \bar{X}_1}(\lambda_1\bar{\sigma}_{\mathrm{h}}) \tag{39}$$

with boundary conditions

$$\bar{J}_1 = \bar{J}_0 \qquad \text{at } \bar{X}_1 = 1,$$
$$\bar{J}_1 = 0 \qquad \text{at } \bar{X}_1 = 0,$$

where

$$\lambda_1\bar{\sigma}_{\mathrm{h}} = \begin{cases} -\bar{E}\dfrac{2\bar{E}\ln\lambda_{\mathrm{Y0}} + 4\bar{E}^{\mathrm{p}}\ln(1+\beta\bar{C})}{3\bar{E}+6(1-\nu)\bar{E}^{\mathrm{p}}}(\lambda_{\mathrm{Y0}})^{\frac{(4\nu-2)\bar{E}}{\bar{E}+2(1-\nu)\bar{E}^{\mathrm{p}}}}(1+\beta\bar{C})^{\frac{3\bar{E}+2(1+\nu)\bar{E}^{\mathrm{p}}}{\bar{E}+2(1-\nu)\bar{E}^{\mathrm{p}}}}, \\ \qquad \text{if } \dfrac{1}{1-\nu}\ln(1+\beta\bar{C}) > \ln\lambda_{\mathrm{Y0}}, \\ -\dfrac{2\bar{E}}{3(1-\nu)}\ln(1+\beta\bar{C})(1+\beta\bar{C})^{\frac{1+\nu}{1-\nu}}, \\ \qquad \text{if } \dfrac{1}{1-\nu}\ln(1+\beta\bar{C}) \leqslant \ln\lambda_{\mathrm{Y0}}. \end{cases} \tag{40}$$

Results from COMSOL and ABAQUS are plotted in figure 2. From figures 2(*a*)–(*d*), normalized lithium concentration, total logarithm strain and logarithm plastic strain along the thickness direction, and the in-plane true stress solved from COMSOL and ABAQUS are plotted for different SOCs, respectively. It is shown that the two sets of solutions from the independent approach agree very well with each other. Thus the numerical implementation embedded in ABAQUS as described in section 3 is benchmarked.

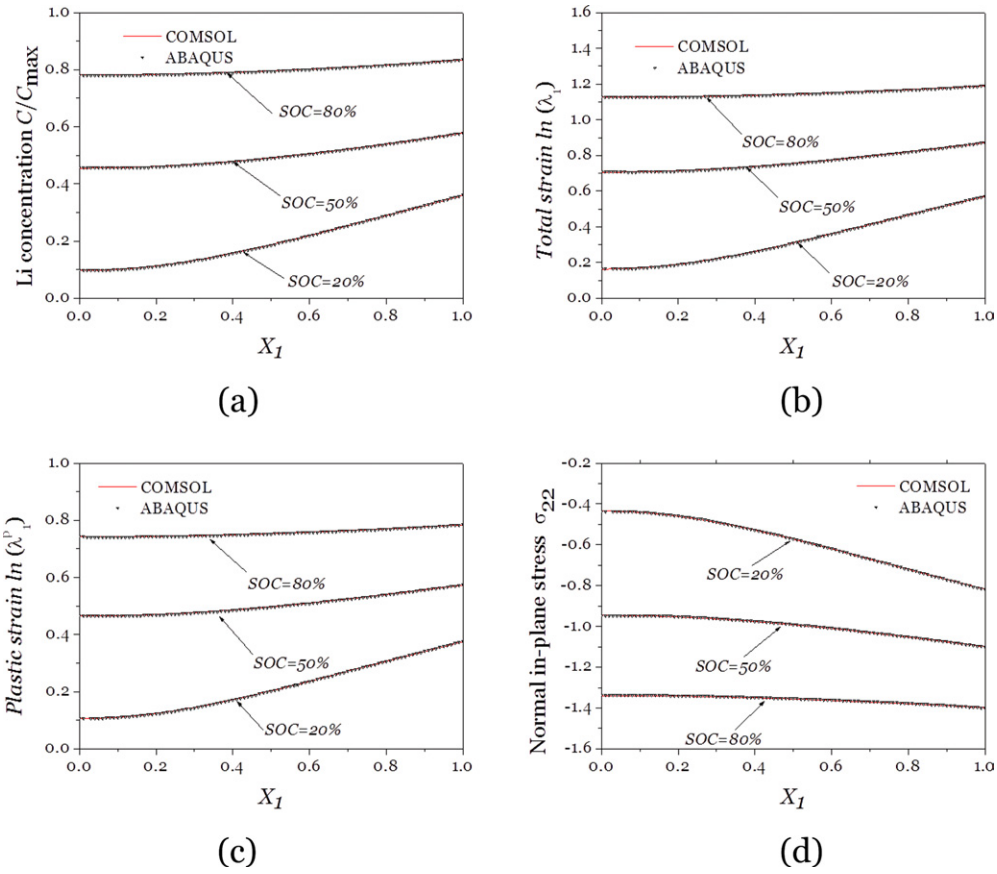

Figure 2. Comparison between the results obtained from the present approach via ABAQUS and COMSOL Multiphysics 4.2: (*a*) normalized concentration, (*b*) total logarithm total strain in the thickness direction, (*c*) logarithm plastic strain in the thickness direction, and (*d*) true in-plane normal stress in the thickness direction at different states of charge (SOC), 20%, 50% and 80%, respectively.

5. Practical examples—capabilities and implications

To demonstrate the capability of the present numerical approach, we study two cases with more practical significance in this section. Figure 3(*a*) shows the problem that we are studying, in which an array of Si patches is patterned as anode material on a copper substrate as the current collector. The configuration of patterned Si patches on substrate has already been used in experiments [51].

5.1. Firmly or compliantly bonded Si on current collector

In this section, we study two cases for different bonding between Si and the current collector. One is that Si is directly and firmly bonded with the current collector and the other one is that there is a compliant and conductive binder between Si and the current collector. In finite elements simulations, the above difference is reflected by the different treatment of the interface between Si and the current collector, as shown in a representative unit cell of this periodical structure in figure 3(*b*) consisting of anode, current collector and the interface. We only study

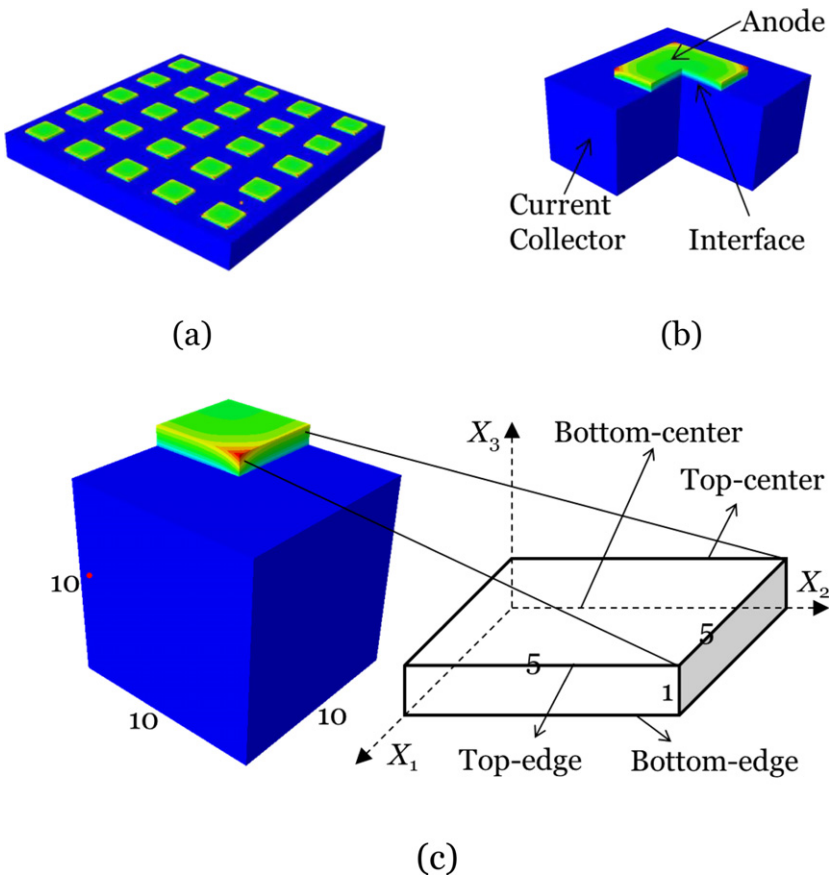

Figure 3. (*a*) Illustration of an array of silicon patches on copper current collector. (*b*) A representative unit. (*c*) A quarter unit used in the finite element simulations with four representative lines defined.

a quarter of the unit as shown in figure 3(*c*) by applying symmetric boundary conditions. Also because of the symmetry, four representative lines in the quarter of the unit, namely top-edge, top-center, bottom-edge and bottom-center are focused in these two cases. All additional parameters used in this section are listed in table 2.

In finite element simulations, the current collector copper is modeled as a linear elastic material with Young's modulus $E_{\mathrm{Cu}} = 110$ GPa and Poisson's ratio $\nu_{\mathrm{Cu}} = 0.34$. The dimension of copper is $10 \times 10 \times 10$, meshed into 8000 ($= 20 \times 20 \times 20$) C3D8R elements. The bottom of the copper ($X_3 = -10$) is fixed and the symmetric boundary conditions are applied on its side surfaces.

The Si anode has the same mechanical properties as discussed in section 4.1, in addition to which the damage of Si is considered here. Due to the lack of experimental data on the damage behavior of Si and that the main point of this section is to demonstrate the capability of the present numerical approach rather than to discuss quantitative physics, we here adopt a simple damage model that is commonly used for metals. We assume that damage is initiated when the equivalent plastic strain $\varepsilon^{\mathrm{pl}}$ reaches a threshold ($\varepsilon^{\mathrm{pl}} = 0.1$ in these two cases). Once damage is initiated, the modulus of Si is subjected to a linear degradation described by the accumulated damage. The evolution of the damage is driven by plastic displacement and the

Table 2. Parameters used in section 5.

Parameters	Values
E_{Cu}, Young's modulus of Cu	110 GPa
ν_{Cu}, Poisson's ratio of Cu	0.34
ε^{pl}, equivalent plastic strain for damage initiation in Si	10%
u^{pl}, maximum plastic displacement for total failure in Si	six times of element size
K_T, tension rigidity of compliant binder	15 GN m^{-1}
K_S, shear rigidity of compliant binder	5 GN m^{-1}
E_{Cr}, Young's modulus of Cr	279 GPa
G_{Cr}, shear modulus of Cr	115 GPa
ε_n^0, ε_s^0, ε_t^0, normal, shear, transverse strain for damage initiation in binder and crack	1%
ε_n^{max}, ε_s^{max}, ε_t^{max}, normal, shear, transverse strain for total failure in binder and crack	10%

failure criterion is the maximum plastic displacement u^{pl} ($u^{pl} = 6$ in these two cases). The dimension of Si is $5 \times 5 \times 1$, meshed into $20 \times 20 \times 4$ C3D20T elements. A constant flux is applied on the top surface of Si.

The interface between Si and current collector is treated differently in the two cases. The firmly bonded case is realized by 'tie' constraint in finite element simulations. The compliant binder between Si and current collector is realized by cohesive elements in ABAQUS. Specifically, we use zero thickness cohesive elements to model the contacting area of 5×5, meshed into one layer of 741 COH3D8 cohesive elements. The traction–separation relation is used to model the cohesive elements. The tension rigidity $K_T = 15\,\text{GN m}^{-1}$ and shear rigidity $K_S = 5\,\text{GN m}^{-1}$ are used, corresponding to a linear material with normalized modulus $\bar{E}_{binder} = 15$ and Poisson's ratio $\nu_{binder} = 0.5$. For the sake of simplicity of simulations, element elimination is not considered here.

Figure 4 provides the profiles of normalized Li concentration (C/C_{max}) and the percentage of the stiffness degradation in the X_2 direction along four representative lines for different SOCs. Figure 4(a) shows that the Li concentration is higher at the outside ($X_2 = 5$) than the inside ($X_2 = 0$) on both top-edge and top-center lines since the outside is more free and less constrained and thus the Li is easier to diffuse in. Going from top-edge to top-center, it is found that the difference in Li concentration from the outside to the inside increases and the absolute value of the Li concentration decreases for the same reason of constraints. The center of the top-edge ($X_2 = 0$) and the edge of the top-center ($X_2 = 5$) occupy the same situation, i.e. with two free surfaces; thus they show the same Li concentrations. For example, normalized Li concentration is 0.91 for the center of the top-edge ($X_2 = 0$) and the edge of the top-center ($X_2 = 5$) when SOC= 60%. Because of the relatively free top surface, the percentage of stiffness degradation is low (only a few per cent), as shown in figure 4(c). Near the edge of the top-edge ($X_2 = 5$), there is even no degradation. This suggests a critical size such that, below this size, the degradation can be avoided on the top surface.

Compared with figure 4(a) where Li concentrations show significant difference between the edge and center, the Li concentrations for the bottom surface, i.e. bottom-edge and bottom-center as in figure 4(b), show less difference, which is a result of the strong constraints at the bottom. Freedom in the lateral direction at the bottom-edge does not provide much advantage in the stress relaxation. The absolute value of the Li concentration on the bottom as a whole is lower than that on the top for the same SOCs. Figure 4(d) shows the percentage of stiffness degradation at the bottom-edge and bottom-center. As we can see, a significant degradation is observed on the bottom-edge. Due to the stress concentration

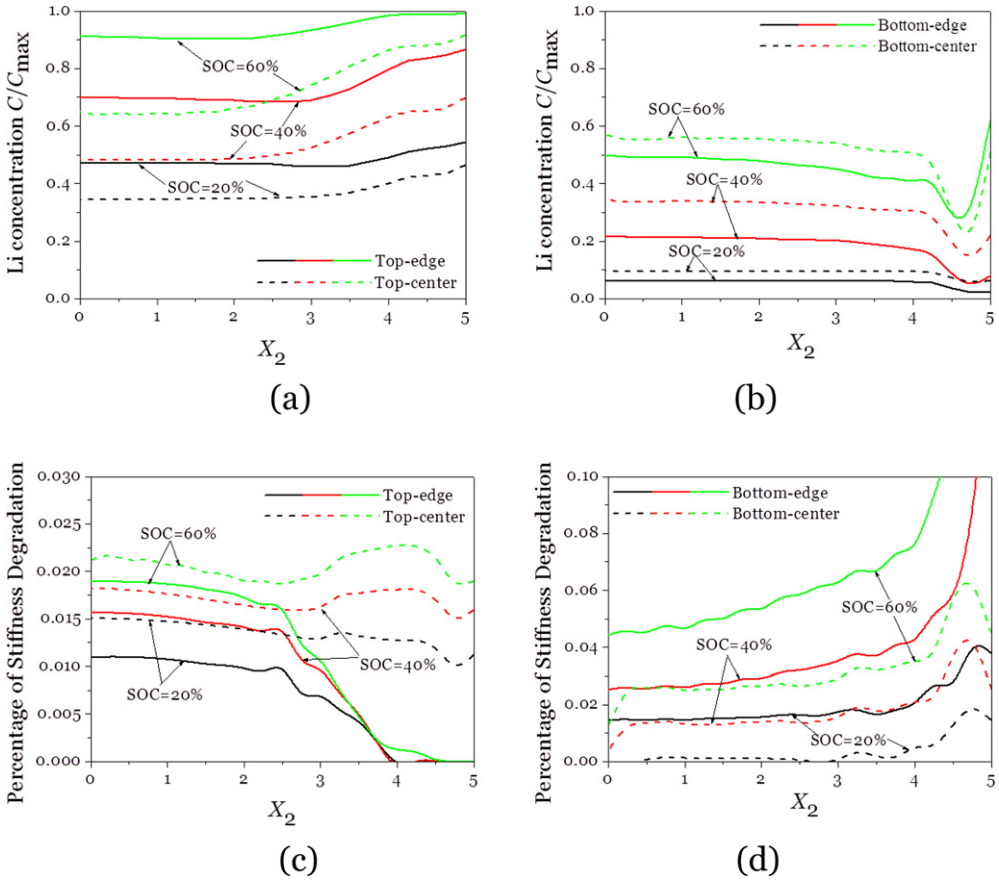

Figure 4. Profiles of normalized lithium concentration (C/C_{max}) (a) and (b) and percentage of stiffness degradation (c) and (d) in the X_2 direction along four representative lines at different SOCs, respectively. The interface between Si and the current collector is firmly bonded.

at the edge of the bottom-edge ($X_2 = 5$), the degradation is even higher, such as over 20% for SOC = 60% according to numerical results (truncated in the figure). Due to the lack of stress concentration at the bottom-center, the percentage of stiffness degradation is not very high, on the order of a few per cent. These results indicate that the bonding between Si and the current collector is a critical point of failure and the failure may start from the corner of the electrode. Solutions to avoid or delay fracture may include electrodes without corners (e.g. round pillar) or compliant binders as to be discussed in the following.

When the bonding between Si and current collector is changed from firmly bonded to elastic binder, the results are very different, as shown in figure 5. Figure 5 provides the profiles of normalized Li concentration (C/C_{max}) and the percentage of the stiffness degradation in the X_2 direction at four representative lines for different SOCs. Figure 5(a) shows that the Li concentration is relatively uniform along both top-edge and top-center, which is very different from the obvious nonuniformly distributed Li shown in figure 4(a). The explanation is that the elastic binder reduces the constraint to the Si anode from the current collector; thus the stress level and its gradient are lower than the case with firmly bonded interface. Without the

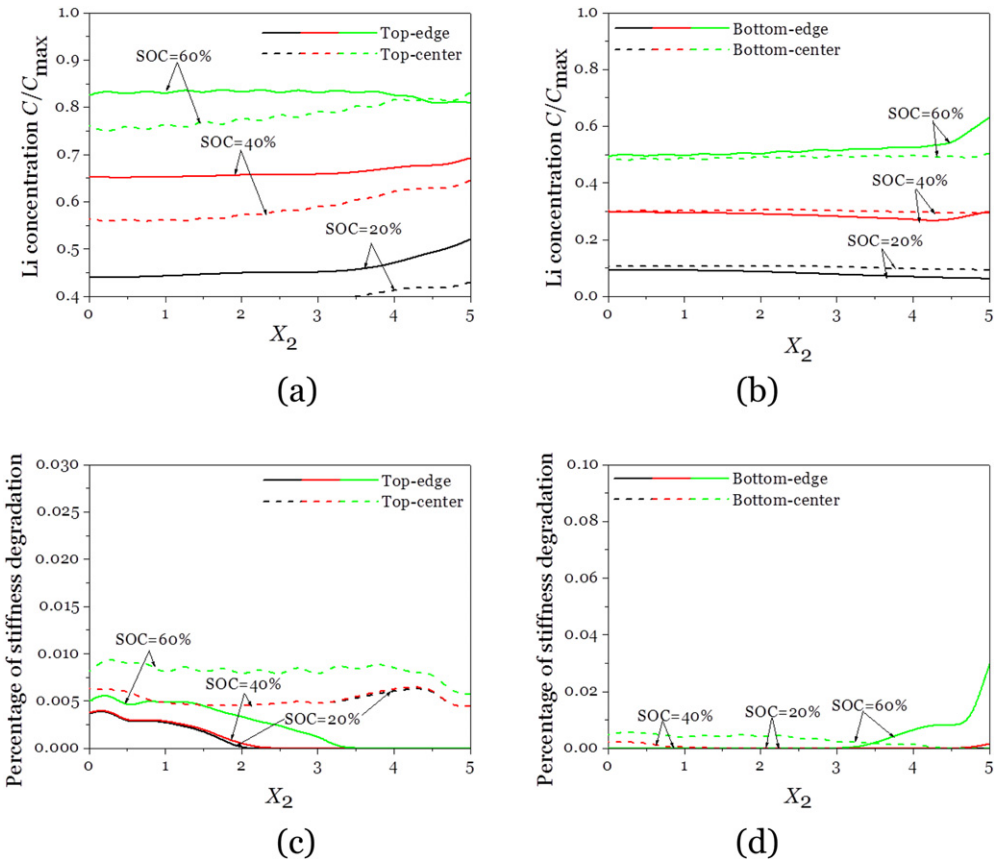

Figure 5. Profiles of normalized lithium concentration (C/C_{max}) (*a*) and (*b*) and percentage of stiffness degradation (*c*) and (*d*) in the X_2 direction along four representative lines at different SOCs, respectively. The interface between Si and the current collector is compliant binder. To compare with the stiffness degradation shown in figures 4(*c*) and (*d*), the same scale is used.

stress and its gradient as driving force for diffusion, diffusion in the X_2 direction thus does not exhibit apparent difference. It is also found from figure 5(*a*) that the Li concentration at the top-edge (solid line) is overall higher than that at the top-center (dashed line) since the top-edge is less constrained. Again, the center of the top-edge ($X_2 = 0$) and the edge of the top-center ($X_2 = 5$) occupy the same situation, i.e. with two free surfaces; thus they show the same Li concentrations. Because the Si is relatively free when the elastic binder is used, the percentage of stiffness degradation for both top-edge and top-center as in figure 5(*c*) is much smaller than that in the case of firmly bonded (figure 4(*c*)). The percentage of stiffness degradation is on the order of 1%. This result suggests that elastic binder can significantly reduce the mechanical degradation of Si anode by creating a more 'free' situation to let Si expand during electrochemical reactions. Thus the cyclic retention can be improved.

Compared with the Li concentration given by figure 5(*a*) for the top surface, the Li concentrations for the bottom surface, i.e. bottom-edge and bottom-center in figure 5(*b*), show similar relatively uniform distribution in the X_2 direction, which is a result of stress relaxation at the bottom. The absolute value of the Li concentration on the bottom as a whole is lower than that on the top for the same SOCs. As shown in figure 5(*d*), the

percentage of stiffness degradation on the bottom surface is much smaller than the case for firmed bonded interface but larger than that on the top surface, because of more constraint on the bottom.

By comparison between the results for firmly bonded interface and elastic binders as interface, it seems to suggest that the elastic bonding is able to help us to homogenize the concentration distribution and mediate the electrode damage, which makes us believe that the cyclic retention of Li-ion batteries can be significantly improved. In fact, elastic binders [52] or similarly elastic substrates [12] have been used in recent experiments and very good cyclic retention has been realized.

5.2. Si bonded on current collector with multiple failure mechanisms

There are two limitations of the cases presented in section 5.1. First, the failure of binders is not considered. Second, Si anodes are assumed intact before lithiation, which does not hold as there are some flaws serving as sites for stress concentration. The interaction between the failure of binders and flaws of Si anodes may provide a variety of failure mechanisms in the anode–binder–collector assembly. In this section, the interplay between different failure mechanisms is studied.

To fulfil the failure in the anode–binder–collector assembly, two modifications are employed in figure 3. First, the failure behavior of the binder that is modeled as a layer of cohesive element is now considered through stiffness degradation. The stiffness degradation is initialized when the nominal strain (either normal strain ε_n, shear strain ε_s or transverse strain ε_t) reaches a critical values, ε_n^0, ε_s^0 or ε_t^0, respectively. Linear damage evolution is assumed and the binder fails completely when the nominal strain reaches the maximum values, ε_n^{max}, ε_s^{max} or ε_t^{max}. In this section, the binder is assumed to be chromium, which is a widely used adhesive material for Si and Cu. The traction–separation relation is given based on Young's modulus and shear modulus of chromium, $E_{Cr} = 279\,GPa$, $G_{Cr} = 115\,GPa$. For simplicity, the criteria for damage initiation are taken as $\varepsilon_n^0 = \varepsilon_s^0 = \varepsilon_t^0 = 1\%$ and those for failure are $\varepsilon_n^{max} = \varepsilon_s^{max} = \varepsilon_t^{max} = 10\%$. 2500 ($= 50 \times 50 \times 1$) COH3D8 elements are used to model the cohesive layer with thickness 0.1. Second, two pre-existing planar cracks are placed in the symmetrical planes of the Si anode, i.e. in the X_1X_3 and X_2X_3 planes, which are also modeled as cohesive elements with vanishing thickness. The traction–separation relation is used for these cohesive elements based on the property of Si. Similar damage initiation and evolution rules are used with $\varepsilon_n^0 = \varepsilon_s^0 = \varepsilon_t^0 = 1\%$ and $\varepsilon_n^{max} = \varepsilon_s^{max} = \varepsilon_t^{max} = 10\%$. 500 ($= 50 \times 10 \times 1$) COH3D8 elements are employed to model each pre-existing crack.

A series of lithiation and delithiation simulations are conducted. Figure 6 shows the contour plots of percentage of stiffness degradation for the two pre-existing cracks and binder at different states of lithiation and delithiation. Figure 7 shows the overall deformation of the Si–binder–collector system at three lithiation/delithiation states listed in figure 6. Before lithiation starts, cracks and binders are not damaged as shown in figure 6(a) where all elements are in blue. During lithiation (figures 6(a)–(f)), damage mainly occurs in the binder and increases monotonically as lithiation. At 90% lithiation (figure 6(f)), the majority of binder has been damaged. The failure of the binder is attributed to the shear between Si patch and copper substrate, which can be observed in figure 7. Figure 7(a) shows the Si–binder–collector assembly before lithiation and figure 7(b) is for the assembly at 50% lithiation. It is obvious that the area of the Si patch increases significantly upon lithiation and bends toward the current collector due to the constraint from it, which leads to great sliding at the interface between the Si patch and the substrate. As observed from figure 6(b), the failure zone initializes from the corner of the binder where the largest sliding occurs. It is also observed that there is no

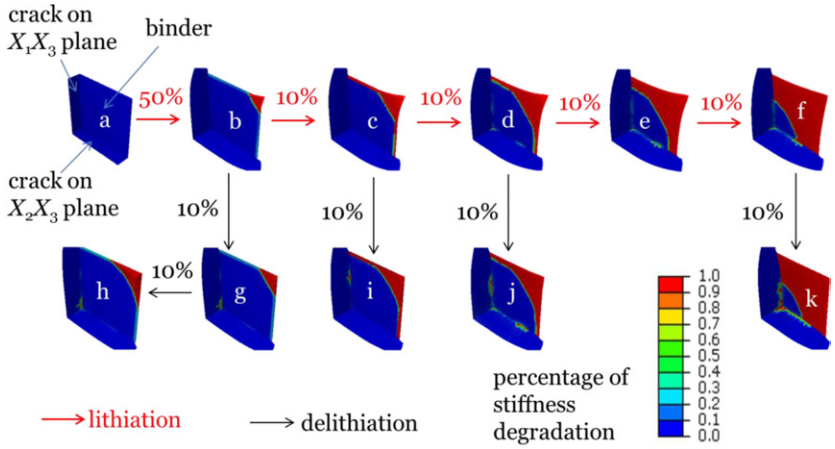

Figure 6. Contour plots of percentage of stiffness degradation in binder and pre-existing cracks at different degrees of lithiation ((*a*)–(*f*)) and delithiation ((*g*)–(*j*)).

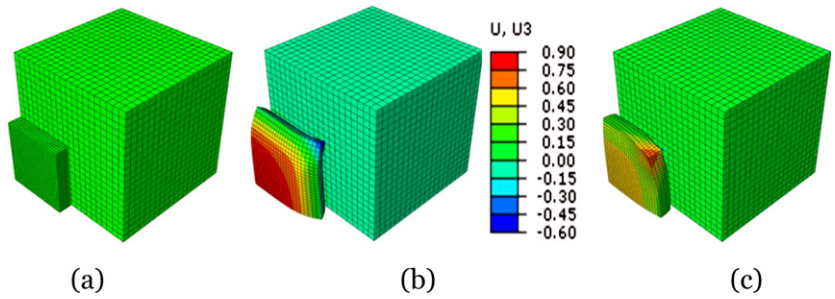

Figure 7. Morphology of the silicon–binder–collector at selected degrees of lithiation/delithiation: (*a*) initial state, (*b*) lithiation state corresponding to figure 6(*b*), and (*c*) delithiation state corresponding to figure 6(*h*).

significant failure in the pre-existing cracks during lithiation since the Si patch is subjected to compressive stress caused by the compositional expansion and constraint from the collector. Figures 6(*g*)–(*k*) show the delithiation processes. It is interesting that there is still no significant failure in the pre-existing cracks, no matter from which state the delithiation starts, at least for 10% and 20% delithiation. This surprising observation is because once the binder is damaged during lithiation, the Si patch above the damaged binder can deform freely and thus 'peeling-off' occurs, which can be seen in figure 7(*c*). Figure 7(*c*) corresponds to the state of delithiation given by figure 6(*h*), in which the corner of the binder has been completely damaged. Therefore, upon delithiation, the Si patch bends against the current collector as a response to the compositional contraction, which leads to compressive stress on the pre-existing cracks and thus prevents damage in the pre-existing cracks. On the other hand, the 'peeling-off' further damages the binder, which is tension controlled and different from the sliding during lithiation.

The results in this section seem to imply that the introduction of damage in some areas of the binder in a controllable way could prevent damage of the active materials. It should be noticed that some parameters (particularly the damage initiation and evolution parameters) are not available yet and chosen in a somewhat arbitrary way. Thus, this section mainly shows the capability and potential of the present numerical approach.

6. Concluding remarks

In this paper, we develop a finite element based numerical method to study the coupled large deformation and diffusion of electrodes in Li-ion batteries under the framework of ABAQUS. The coupling is realized by an analogy between diffusion and thermal transfer in ABAQUS. Due to the large deformation, this analogy is rigorously examined and the corresponding relation is established. It is found that this formulation is able to realize the coupled deformation and diffusion in large deformation using several user-defined subroutines in ABAQUS, namely user-defined thermal transport (UMATHT), user-defined flux (UFLUX) and user-defined expansion (UEXPAN). Because the present formulation does not involve any element development in ABAUQS, many built-in modules can be directly utilized. A system comprising three components, namely, Si electrode, binder and current collector, is studied using the cohesive elements and the damage to the electrode is considered. It is anticipated that this formulation is able to model many coupled large deformation and diffusion problems in electrodes with complex spatial and temporal conditions, such as damage evolution, fracture and electrodes/binder delamination, among others. When this formulation is combined with experimental work, it is expected that the constitutive relations (e.g. stress versus SOC) can be extracted from various techniques, such as micro-indentation.

We here have to emphasize again that the results presented in this paper by no means intend to explain the real mechanisms occurred in the electrodes during electrochemical reactions. The main point of this paper is to examine a rigorous implementation of coupled deformation and diffusion through a commonly used coupled deformation and heat transfer when the extremely large deformation presents. When the theoretical model is changed, the implementation can be revised correspondingly. However, since the major field variables are used in the present implementation, such as stress, deformation gradient, concentration and their gradient, the modification of the implementation is fairly straightforward.

Acknowledgments

The authors appreciate the High Performance Computing Initiative (HPCI) at the Arizona State University. YA acknowledges the financial support from the China Scholarship Council. HJ acknowledges the support from NSF CMMI-1067947 and CMMI-1162619.

Appendix A. Implementation of UMATHT

In the subroutine UMATHT, the standard parameters received from ABAQUS are temperature T and its spatial gradient at the current state $\partial T/\partial x_i$, or equivalently, $\bar{C}$ and $\partial \bar{C}/\partial \bar{x}_i$ using the analogy discussed in section 3.2, respectively. The variables that are needed to pass out to ABAQUS are heat capacity per volume $\rho(\mathrm{d}U/\mathrm{d}T)$, heat flux f_i and its derivatives respective to temperature $\partial f_i/\partial T$ and temperature gradient $\partial f_i/\partial(\partial T/\partial x_i)$.Using the analogy discussed in section 3.2, the output variables in UMATHT are $1/\det(\boldsymbol{F})$ (for $\rho(\mathrm{d}U/\mathrm{d}T)$), $F_{iK}\bar{J}_K/\det \boldsymbol{F}$ (for f_i), $(\partial/\partial\bar{C})(F_{iK}\bar{J}_K/\det \boldsymbol{F})$ (for $\partial f_i/\partial T$), and $\partial(F_{iK}\bar{J}_K/\det \boldsymbol{F})/\partial(\partial\bar{C}/\partial\bar{x}_i)$ (for $\partial f_i/\partial(\partial T/\partial x_i)$). The flux $\bar{J}_K$ depends on deformation gradient $\boldsymbol{F}$, stress σ, and second Piolar–Kirchhoff stress $\boldsymbol{S}$, as shown in equation (24). Therefore, the implementation of UMATHT also needs to access the deformation gradient $\boldsymbol{F}$ and stress σ (and $\boldsymbol{S}$) and to calculate their derivatives (specifically, $\partial(\det \boldsymbol{F}\bar{\sigma}_{\mathrm{h}})/\partial\bar{X}_L$ in equation (24)), which are not the standard parameters received from ABAQUS.

The access of deformation gradient $\boldsymbol{F}$ can be realized by a 'dummy' user-defined material subroutine UMAT. Here the 'dummy' indicates that this subroutine UMAT does not actually

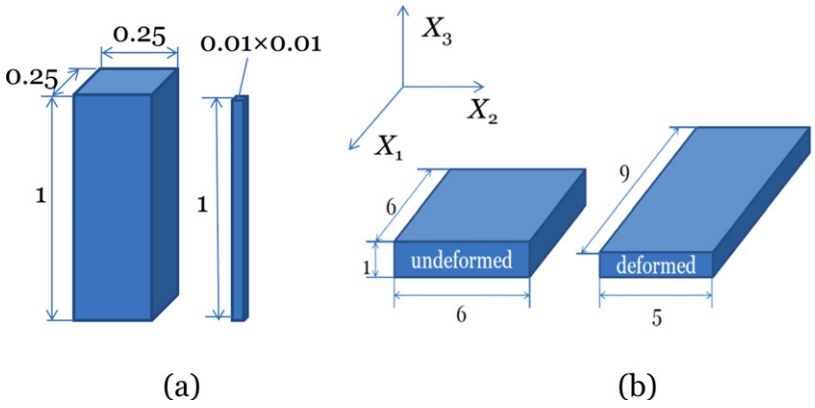

Figure A1. (*a*) Models used to examine the calculation of $\partial/\partial\bar{X}_3(\det(\boldsymbol{F})\bar{\sigma}_{\mathrm{h}})$ in UMATHT in appendix A, fat square pillar used to compare the shape function extrapolation (SFE) method and the PLS method, and thin square pillar used to examine the 'gradient calculation window' in PLS method. (*b*) Models used in the benchmark examples in appendix B, an undeformed thin plate with geometry $6 \times 6 \times 1$ and a deformed thin plate with geometry $9 \times 5 \times 1$. The deformation is prescribed as $x_1 = 1.5X_1$, $x_2 = 5X_2/6$.

perform any calculations but access the deformation gradient $\boldsymbol{F}$ from ABAQUS since UMAT is one of the two ways in ABAQUS that can retrieve the deformation gradient $\boldsymbol{F}$ (UHYPER is another way). The stress tensor is obtained using another ABAQUS subroutine USDFLD, user-defined field variables. The accessed deformation gradient $\boldsymbol{F}$ and stress are given for every integration point and passed to the subroutine UMATHT.

In addition to deformation gradient $\boldsymbol{F}$ and stress in UMATHT, the gradients of $\det(\boldsymbol{F})\bar{\sigma}_{\mathrm{h}}$ with respect to the reference coordinates $\boldsymbol{X}$ need to be calculated, which is the main challenge here. In the finite element method, the calculation of derivatives is realized through the shape function that interpolates a nodal value of a variable to its value at the integration point. However, here the deformation gradient $\boldsymbol{F}$ and stress are given at the integration points, not at the nodal points. We have implemented two ways to calculate this gradient $(\partial/\partial\bar{X}_L)(\det(\boldsymbol{F})\bar{\sigma}_{\mathrm{h}})$.

The first way is the shape function extrapolation (SFE) method. $\det(\boldsymbol{F})\bar{\sigma}_{\mathrm{h}}$is calculated at all integration points within an element. Then these values at the integration points are extrapolated to their nodes using the inverse of a certain shape function (depending on the type of element). Once the nodal value of $\det(\boldsymbol{F})\bar{\sigma}_{\mathrm{h}}$ is known, the derivatives at the integration points are calculated using the same shape function. It could be proved that this algorithm is equivalent to the spatial finite difference method. Although this method is straightforward, two drawbacks exist. One shortcoming is that this method is element dependent because of the shape function, which involves more efforts to implement this method for different types of elements. The second one is more critical. The present method of calculating derivatives only involves local information within one element, which causes unrealistic gradients even when the deformation and stress fields are relatively smooth throughout a few neighboring elements. This unrealistic gradient fluctuates and makes the convergence difficult.

The second way is to calculate this gradient using the PLS method. In order to calculate $(\partial/\partial\bar{X}_L)(\det(\boldsymbol{F})\bar{\sigma}_{\mathrm{h}})$ of an integration point, we first select a 'gradient calculation window' that contains a few elements around it. Within this window, $\det(\boldsymbol{F})\bar{\sigma}_{\mathrm{h}}$ is assumed to be distributed linearly, i.e.

$$\det(\boldsymbol{F})\bar{\sigma}_{\mathrm{h}}(\bar{X}_K) = a_0 + a_1\bar{X}_1 + a_2\bar{X}_2 + a_3\bar{X}_3, \tag{A1}$$

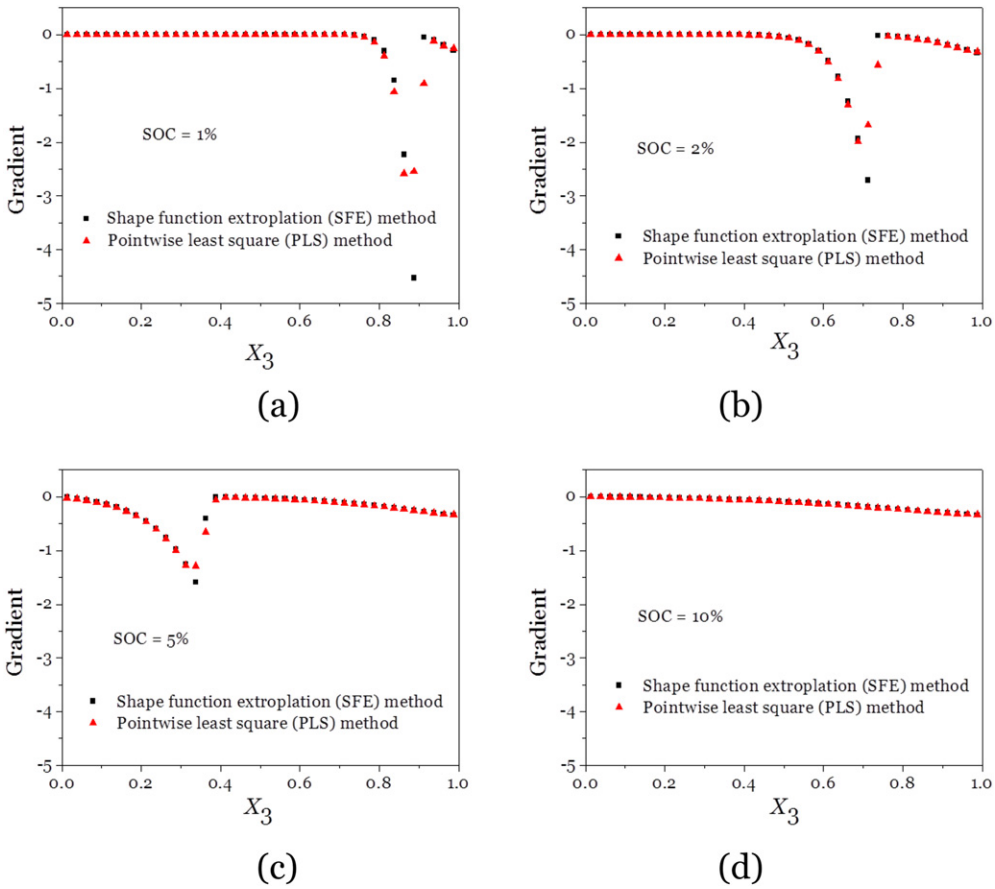

Figure A2. Gradient $\partial/\partial\bar{X}_3(\det(\boldsymbol{F})\bar{\sigma}_{\mathrm{h}})$ profile in the X_3 direction at different SOC, calculated from shape function extrapolation (SFE) and PLS methods. SOCs are (*a*) 1%, (*b*) 2%, (*c*) 5% and (*d*) 10%, respectively. Here the dimensionless time is used.

where $\bar{X}_K$ are the initial coordinates of an integration point within the 'gradient calculation window' and $\det(\boldsymbol{F})\bar{\sigma}_{\mathrm{h}}(\bar{X}_K)$ is the value of this function at $\bar{X}_K$, and $a_i (i = 0, 1, 2, 3)$ are four unknown polynomial coefficients to be determined using the least squares method. The gradient $(\partial/\partial\bar{X}_L)(\det(\boldsymbol{F})\bar{\sigma}_{\mathrm{h}})$ at an integration point can therefore be calculated based on the obtained coefficients a_1, a_2 and a_3.Since this method involves non-local information, compared to the first method that only uses the local information within one element, the fluctuation of the gradient can be largely removed and the accuracy of the gradient can be greatly improved. This method has been used in obtaining meaningful strain field from measured displacement field in digital image correlation (DIC) [53].

As sketched in figure A1(*a*), a Si pillar with a square cross section is used. The pillar geometry is $0.25 \times 0.25 \times 1$. The pillar is charged by a unit flux with lateral displacement totally confined. The material parameters involved are the same as listed in section 4.1 and $4 \times 4 \times 40$ C3D20T elements are used to mesh this pillar. Figure A2 compares the gradient $(\partial/\partial\bar{X}_L)(\det(\boldsymbol{F})\bar{\sigma}_{\mathrm{h}})$ calculated from SFE and PLS methods at different SOC. In the SFE method, the standard quadratic shape function of C3D20T element is used; while for the PLS method, averaging over second-order neighboring elements is adopted. It is found that the gradients calculated from these two methods are very close. However, the gradient from the

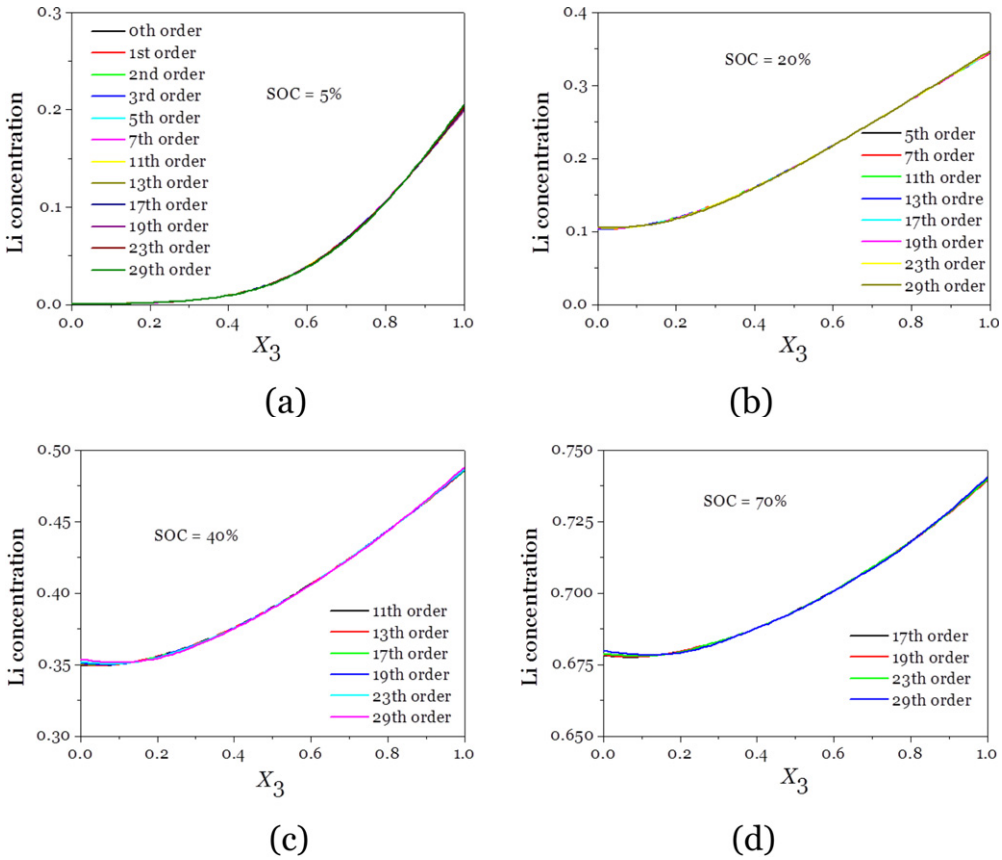

Figure A3. The profile of Li concentration in the X_3 direction at different SOCs using various 'gradient calculation windows'. The SOCs are (*a*) 5%, (*b*) 20%, (*c*) 40% and (*d*) 70%.

PLS method is always smoother than that from the SFE method, which usually make the convergence easier in most of our simulations.

It is important to note that to obtain reasonable and accurate gradients$(\partial/\partial\bar{X}_L)(\det(\boldsymbol{F})\bar{\sigma}_{\mathrm{h}})$ using the PLS method, the size of 'gradient calculation window' is critical. There is a trade-off between the accuracy and smoothness of the gradient. Figure A3 shows a case study on the effect of 'gradient calculation window' using an example of charging a laterally confined slender Si pillar (figure A1(*a*)). The dimensions are $0.01 \times 0.01 \times 1$ and the mesh is $1 \times 1 \times 100$. A unit flux is applied on the top surface. The material properties are given in section 4.1. The 'gradient calculation window' is defined by the number of neighboring element, i.e. '0' means the element itself, '1' means the first-order neighboring elements and so on. The profiles of Li concentration in the X_3 direction at different SOCs are shown in figure A3. The results show that for this relatively homogeneous deformation (1D problem), the size of 'gradient calculation window' is insignificant. The difference only lies in the efficiency of convergence, namely, small 'window' leads to much slower convergence rate than that for larger 'window'. The calculations presented in this paper normally use second-order or third-order neighboring elements to conduct the PLS method.

With all the necessary quantities accessed and calculated, the mass diffusion in large deformation is implemented in UMATHT through the analogy discussed in section 3.2.

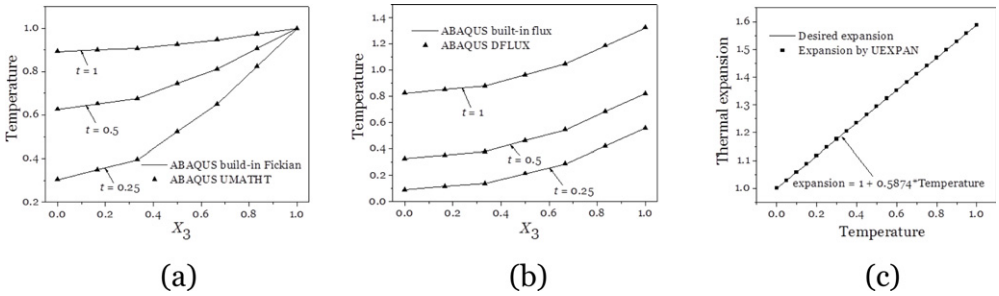

Figure A4. Benchmark of numerical implementation in user subroutines. (*a*) Upon applying a prescribed temperature boundary condition, temperature profiles in the X_3 direction at different time steps, using ABAQUS built-in thermal transport with Fickian law and ABAQUS UMATHT by expressing the total Lagrange description in updated Lagrange framework via equation (26). (*b*) Upon applying a prescribed flux boundary condition, temperature profiles in the X_3 direction at different time steps, using ABAQUS built-in heat transfer/flux boundary condition and ABAQUS UMATHT/DLFUX via equations (26) and (35). (*c*) Thermal expansion versus temperature for a static state problem, by increasing the temperature from 0 to 1, using ABAQUS UEXPAN. The coefficient of expansion is taken to be 0.5874 and thus large deformation due to elevated temperature is introduced.

Appendix B. Benchmark examples

Several benchmark examples are conducted to show the correct implementation of all aspects discussed in section 3.

Figure A1(*b*) illustrates a thin-film model used in the benchmark studies. The X_3-axis is normal to the film and the X_1- and X_2-axes are along the in-plane direction. The thickness of the film is set to 1. To illustrate that the large deformation can be correctly captured, a large deformation, $x_1 = 1.5X_1$, $x_2 = 5X_2/6$, is applied to the undeformed configuration to deform it to the deformed one shown in figure A1(*b*). We use 27 C3D8T elements in the benchmark studies.

B.1. Benchmark updated Lagrange and total Lagrange descriptions on the same problem

The analogy between mass diffusion and heat transfer in ABAQUS relies on one basic foundation, which is the mass conservation law for diffusion in the total Lagrange description (equation (23)) is equivalent to the heat conservation law for heat transfer in the updated Lagrange description (equation (25)) through equation (26). To verify that this equivalence does describe the same physics, we create two scenarios. In the first scenario, we just use ABAQUS built-in Fickian diffusion to study a pure heat transfer problem, i.e. without thermal expansion and mechanical deformation. The model is shown on the left side in figure A1(*b*). The top surface is subjected to a prescribed unit temperature for a unit time. Thus, the governing equation in this case is equation (25). In the second scenario, we apply large deformation and then conduct the heat transfer. The model is shown on the right side in figure A1(*b*). This deformation is uniform, which can be accurately described by these 27 elements used in the example. The boundary condition for heat transfer is the same as that in the first scenario. In this analysis, the large deformation option is on and the deformation gradient can be accessed using the 'dummy' UMAT subroutine as discussed in appendix A. The conservation law is described in the total Lagrange framework, which is similar to equation (23). We implement equation (23) in the updated Lagrange framework using equation (26) in UMATHT. These two scenarios solve a pure heat transfer problem since the deformation and heat transfer are

intentionally decoupled. Figure A4(*a*) shows that the temperature profiles in the X_3 direction for these two scenarios are identical for several time steps, which verifies the realization of total Lagrange description in updated Lagrange framework via equation (26).

B.2. Benchmark prescribed flux boundary condition

Still because of the discrepancy between total Lagrange and updated Lagrange descriptions, flux is applied on different elements of area in these two descriptions. This discrepancy can be eliminated using Nanson's formula as discussed in equation (35). We still create two scenarios to benchmark. The first scenario is similar to the first case in B1, except that the prescribed temperature boundary condition is replaced by a prescribed flux boundary condition. Specifically, the top surface of the film is subjected to a unit heat flux for a unit time. The same prescribed flux boundary condition and the deformation field are applied in the second scenario. To accommodate the change of the area on the top surface, subroutine DFLUX is used in the second scenario along with UMATHT for the heat conservation law defined in updated Lagrange framework when large deformation presents. It should be emphasized here again that these two cases are temperature–deformation decoupled. The deformation is introduced solely in order to show that a proper transformation between total Lagrange and updated Lagrange framework is needed to correctly describe the physics. Figure B4(*b*) shows that the temperature profiles in the X_3 direction at different time steps for these two scenarios are identical, which verifies the implementation of DFLUX to capture the flux when large deformation presents.

B.3. Benchmark thermal expansion for large deformation

For large deformation, the thermal expansion needs to be redefined to realize the desired compositional expansion (equation (29)) through equation (33). We study a steady-state problem by increasing the temperature from zero to unity and the compositional expansion coefficient $\beta = 0.5874$. The thermal expansion is redefined in UEXPAN via equation (33). As shown in figure A4(*c*), a desired linear expansion is produced. The slope is just the compositional expansion β $(= 0.5874)$.

Appendix C. Analytical solution for deformation in a 1D problem

As illustrated in figure 1(*b*), the substrate is assumed rigid. Due to the symmetry of the problem, there are five independent field variables $\lambda_1^{\mathrm{e}}(X_1, t)$, $\lambda_2^{\mathrm{e}}(X_1, t)$, $\lambda_1^{\mathrm{p}}(X_1, t)$, $\lambda_2^{\mathrm{p}}(X_1, t)$ and $\bar{C}(X_1, t)$.

From the incompressibility of plastic deformation

$$\ln\left(\lambda_1^{\mathrm{p}}\lambda_2^{\mathrm{p}}\lambda_2^{\mathrm{p}}\right) = 0, \tag{C1}$$

and the fixed in-plane displacement condition imposed by a rigid substrate

$$\lambda_2 = 1, \tag{C2}$$

as well as the traction-free condition in the thickness direction

$$\sigma_1 = 0, \tag{C3}$$

one obtains

$$\ln \lambda_2^{\mathrm{p}} = -\ln \lambda_2^{\mathrm{e}} - \ln(1 + \beta\bar{C}), \tag{C4}$$

$$\ln \lambda_{\mathrm{eq}}^{\mathrm{p}} = 2|\ln \lambda_2^{\mathrm{p}}|. \tag{C5}$$

In addition, from the traction-free condition in the thickness direction and the elastic constitutive relations, one can reach

$$\sigma_2 = \frac{E}{1-\nu} \ln \lambda_2^{\mathrm{e}}, \tag{C6}$$

$$\sigma_v = \frac{E}{1-\nu} |\ln \lambda_2^{\mathrm{e}}|. \tag{C7}$$

Substituting the von Mises stress and equivalent strain into the yielding criterion, one obtains

$$\frac{E}{1-\nu} |\ln \lambda_2^{\mathrm{e}}| = \sigma_{\mathrm{Y0}} + 2E^{\mathrm{p}} |\ln \lambda_2^{\mathrm{p}}|. \tag{C8}$$

During lithiation, there is no unloading and the film is subjected to lateral compressive stress, which gives

$$\ln \lambda_2^{\mathrm{e}} \leqslant 0, \qquad \ln \lambda_2^{\mathrm{p}} \leqslant 0. \tag{C9}$$

Then equation (C8) leads to

$$-\frac{E}{1-\nu} \ln \lambda_2^{\mathrm{e}} = E \ln \lambda_{\mathrm{Y0}} + 2E^{\mathrm{p}} (\ln \lambda_2^{\mathrm{e}} + \ln(1+\beta\bar{C})), \tag{C10}$$

from which all four independent deformation fields could be determined as a function of $\bar{C}$ in the following

$$\ln \lambda_2^{\mathrm{e}} = -\frac{(1-\nu)E \ln \lambda_{\mathrm{Y0}} + 2(1-\nu)E^{\mathrm{p}} \ln(1+\beta\bar{C})}{E + 2(1-\nu)E^{\mathrm{p}}}, \tag{C11}$$

$$\ln \lambda_1^{\mathrm{e}} = \frac{2\nu E \ln \lambda_{\mathrm{Y0}} + 4\nu E^{\mathrm{p}} \ln(1+\beta\bar{C})}{E + 2(1-\nu)E^{\mathrm{p}}}, \tag{C12}$$

$$\ln \lambda_2^{\mathrm{p}} = \frac{(1-\nu)E \ln \lambda_{\mathrm{Y0}} - E \ln(1+\beta\bar{C})}{E + 2(1-\nu)E^{\mathrm{p}}}, \tag{C13}$$

$$\ln \lambda_1^{\mathrm{p}} = \frac{-2(1-\nu)E \ln \lambda_{\mathrm{Y0}} + 2E \ln(1+\beta\bar{C})}{E + 2(1-\nu)E^{\mathrm{p}}}. \tag{C14}$$

Two dependent variables which explicitly enter the governing equation for the diffusion problem could be calculated as

$$\sigma_{\mathrm{h}} = -E \frac{2E \ln \lambda_{\mathrm{Y0}} + 4E^{\mathrm{p}} \ln(1+\beta\bar{C})}{3E + 6(1-\nu)E^{\mathrm{p}}}, \tag{C15}$$

$$\ln \lambda_1 = \frac{-(2-4\nu)E \ln \lambda_{\mathrm{Y0}} + (3E + (2+2\nu)E^{\mathrm{p}}) \ln(1+\beta\bar{C})}{E + 2(1-\nu)E^{\mathrm{p}}}. \tag{C16}$$

Aforementioned formulae hold for plastic deformation, which is specified by the condition of yielding

$$\frac{1}{1-\nu} \ln(1+\beta\bar{C}) > \ln \lambda_{\mathrm{Y0}}. \tag{C17}$$

The formulae for elastic deformation can be degenerated from the plastic solution by simply taking $E^{\mathrm{p}} \to \infty$.

References

[1] Narri G-A and Pistoia G 2004 *Lithium Batteries: Science and Technology* (Berlin: Springer)
[2] Armand M and Tarascon J M 2008 Building better batteries *Nature* **451** 652–7
[3] Tarascon J M and Armand M 2001 Issues and challenges facing rechargeable lithium batteries *Nature* **414** 359–67
[4] Chan C K *et al* 2008 High-performance lithium battery anodes using silicon nanowires *Nature Nanotechnol.* **3** 31–5
[5] Boukamp B A, Lesh G C and Huggins R A 1981 All-solid lithium electrodes with mixed-conductor matrix *J. Electrochem. Soc.* **128** 725–9
[6] Hatchard T D and Dahn J R 2004 *In situ* XRD and electrochemical study of the reaction of lithium with amorphous silicon *J. Electrochem. Soc.* **151** A838–42
[7] Cui L F *et al* 2010 Light-weight free-standing carbon nanotube–silicon films for anodes of lithium ion batteries *Acs Nano* **4** 3671–8
[8] Cui L F *et al* 2009 Crystalline–amorphous core–shell silicon nanowires for high capacity and high current battery electrodes *Nano Lett.* **9** 491–5
[9] Park M H *et al* 2009 Silicon nanotube battery anodes *Nano Lett.* **9** 3844–7
[10] Chan C K *et al* 2009 Structural and electrochemical study of the reaction of lithium with silicon nanowires *J. Power Sources* **189** 34–9
[11] Lee S J *et al* 2001 Stress effect on cycle properties of the silicon thin-film anode *J. Power Sources* **97–98** 191–3
[12] Yu C *et al* 2012 Silicon thin films as anodes for high-performance lithium-ion batteries with effective stress relaxation *Adv. Energy Mater.* **2** 68–73
[13] Sethuraman V A *et al* 2010 *In situ* measurements of stress evolution in silicon thin films during electrochemical lithiation and delithiation *J. Power Sources* **195** 5062–6
[14] Sethuraman V A *et al* 2010 *In situ* measurements of stress-potential coupling in lithiated silicon *J. Electrochem. Soc.* **157** A1253–61
[15] Prussin S 1961 Generation and distribution of dislocations by solute diffusion *J. Appl. Phys.* **32** 1876–81
[16] Li J C M 1978 *Metall. Trans.* A **9** 1353–80
[17] Wang W L, Lee S and Chen J R 2002 *J. Appl. Phys.* **91** 9584–90
[18] Yang, F 2005 *Mater. Sci. Eng.* A **409** 153–9
[19] Swaminathan N, Qu J and Sun Y 2007 An electrochemomechanical theory of defects in ionic solids: I. Theory *Phil. Mag.* **87** 1705–21
[20] Swaminathan N, Qu J and Sun Y 2007 An electrochemomechanical theory of defects in ionic solids: II. Examples *Phil. Mag.* **87** 1723–42
[21] Haftbaradaran H *et al* 2011 Continuum and atomistic models of strongly coupled diffusion, stress, and solute concentration *J. Power Sources* **196** 361–70
[22] Haftbaradaran H, Gao H J and Curtin W A 2010 A surface locking instability for atomic intercalation into a solid electrode *Appl. Phys. Lett.* **96** 3
[23] Zhao K *et al* 2012 Reactive flow in silicon electrodes assisted by the insertion of lithium *Nano Lett.* **12** 4397–403
[24] Zhao K *et al* 2011 Lithium-assisted plastic deformation of silicon electrodes in lithium-ion batteries: a first-principles theoretical study *Nano Lett.* **11** 2962–7
[25] Zhao K J *et al* 2011 Large plastic deformation in high-capacity lithium-ion batteries caused by charge and discharge *J. Am. Ceram. Soc.* **94** S226–35
[26] Bower A F, Guduru P R and Sethuraman V A 2011 A finite strain model of stress, diffusion, plastic flow, and electrochemical reactions in a lithium-ion half-cell *J. Mech. Phys. Solids* **59** 804–28
[27] Zhao K *et al* 2012 Fracture and debonding in lithium-ion batteries with electrodes of hollow core–shell nanostructures *J. Power Sources* **218** 6–14
[28] Zhang J P *et al* 2009 A finite element method for transient analysis of concurrent large deformation and mass transport in gels *J. Appl. Phys.* **105** 093522
[29] Kang M K and Huang R 2010 A variational approach and finite element implementation for swelling of polymeric hydrogels under geometric constraints *J. Appl. Mech.—Trans. ASME* **77** 061004
[30] Hong W, Liu Z S and Suo Z G 2009 Inhomogeneous swelling of a gel in equilibrium with a solvent and mechanical load *Int. J. Solids Struct.* **46** 3282–9
[31] Gao Y F and Zhou M 2012 Strong stress-enhanced diffusion in amorphous lithium alloy nanowire electrodes *J. Appl. Phys.* **109** 014310
[32] Yang H *et al* 2012 Orientation-dependent interfacial mobility governs the anisotropic swelling in lithiated silicon nanowires *Nano Lett.* **12** 1953–8
[33] Ryu I *et al* 2011 Size-dependent fracture of Si nanowire battery anodes *J. Mech. Phys. Solids* **59** 1717–30

[34] Haftbaradaran H *et al* 2010 Continuum and atomistic models of strongly coupled diffusion, stress, and solute concentration *J. Power Sources* **196** 361–70
[35] Liu X H *et al* 2011 Anisotropic swelling and fracture of silicon nanowires during lithiation *Nano Lett.* **11** 3312–8
[36] Cui Z W, Gao F and Qu J M 2012 A finite deformation stress-dependent chemical potential and its applications to lithium ion batteries *J. Mech. Phys. Solids* **60** 1280–95
[37] Koretsky M D 2004 *Engineering and Chemical Thermodynamics* (New York: Wiley)
[38] Wang J W *et al* 2013 Two-phase electrochemical lithiation in amorphous silicon *Nano Lett.* **13** 709–15
[39] Liu X H *et al* 2011 Ultrafast electrochemical lithiation of individual Si nanowire anodes *Nano Lett.* **11** 2251–8
[40] McDowell M T *et al* 2013 *In situ* TEM of two-phase lithiation of amorphous silicon nanospheres *Nano Lett.* **13** 758–64
[41] Lee S W *et al* 2011 Anomalous shape changes of silicon nanopillars by electrochemical lithiation *Nano Lett.* **11** 3034–9
[42] Hong W and Wang X 2013 A phase-field model for systems with coupled large deformation and mass transport *J. Mech. Phys. Solids* **61** 1281–94
[43] Cui Z W *et al* 2012 A second nearest-neighbor embedded atom method interatomic potential for Li–Si alloys *J. Power Sources* **207** 150–9
[44] Brassart L and Suo Z G 2013 Reactive flow in solids *J. Mech. Phys. Solids* **61** 61–77
[45] Cui Z W, Gao F and Qu J M 2013 Interface-reaction controlled diffusion in binary solids with applications to lithiation of silicon in lithium-ion batteries *J. Mech. Phys. Solids* **61** 293–310
[46] Bower A F and Guduru P R 2012 A simple finite element model of diffusion, finite deformation, plasticity and fracture in lithium ion insertion electrode materials *Modelling Simul. Mater. Sci. Eng.* **20** 045004
[47] INSPEC 1988 *Properties of Silicon* (New York: Institution of Electrical Engineers)
[48] Sethuraman V A *et al* 2011 *In situ* measurements of stress evolution in silicon thin films during electrochemical lithiation and delithiation *J. Power Sources* **195** 5062–6
[49] Ruffo R *et al* 2009 Impedance analysis of silicon nanowire lithium ion battery anodes *J. Phys. Chem.* C **113** 11390–8
[50] Dimov N *et al* 2003 Characterization of carbon-coated silicon: structural evolution and possible limitations *J. Power Sources* **114** 88–95
[51] Haftbaradaran H *et al* 2012 Method to deduce the critical size for interfacial delamination of patterned electrode structures and application to lithiation of thin-film silicon islands *J. Power Sources* **206** 357–66
[52] Liu G *et al* 2011 Polymers with tailored electronic structure for high capacity lithium battery electrodes *Adv. Mater.* **23** 4679–83
[53] Pan B *et al* 2009 Digital image correlation using iterative least squares and pointwise least squares for displacement field and strain field measurements *Opt. Lasers Eng.* **47** 865–74